ASCE

Discrete-Element Method Simulations of the Seismic Response of Flexible Retaining Walls

Saman Farzi Sizkow[1] and Usama El Shamy, M.ASCE[2]

Abstract: In this study, an analysis of soil–retaining wall dynamic interaction is conducted using three-dimensional discrete-element method (DEM) simulations. Soil grains are treated as rigid spherical particles that are allowed to overlap one another at contact points. The flexible sheetpile-type retaining wall is simulated using rigid balls glued together by parallel bonds with specific strength and stiffness to mimic the physical properties and stiffness of a real wall. Owing to computational limitations, the high *g*-level concept and scaling laws for dynamic centrifuge testing are utilized to decrease the domain size and simulation time. In addition, free-field boundaries are employed at the lateral sides of the model to prevent the reflections of the propagating waves back to the assembly and enforce free-field motion. Seismic excitation is introduced to the system through the base wall, which represents the bedrock. The effects of different characteristics of the input seismic wave, such as its frequency and amplitude, on the dynamic response of the soil–sheetpile system are analyzed. Furthermore, data on the lateral thrust and bending moment on the wall and its deflection are collected. It is found that the lateral earth pressure and bending moment increase during seismic excitation and the final residual values are, in most cases, considerably larger than the initial static ones. It is also observed that the maximum amplification of ground acceleration behind the sheetpile, the amount of wall deformation, and the maximum level of internal forces and moments the sheetpile experiences during dynamic loading are strongly affected by the frequency and amplitude of the input motion. The results show that for ground acceleration stronger than a critical limit, the maximum lateral earth pressure stays almost at a constant level. However, the maximum dynamic bending moment on the wall is found to increase even for ground accelerations higher than the critical value. **DOI: 10.1061/(ASCE)GT.1943-5606.0002428.**

Introduction

Earthquakes can cause serious damage to retaining walls, which may include tilting or sliding of the walls. In addition, these wall movements can cause severe damage to neighboring structures. Many reports have documented damage to retaining walls during earthquakes (Grivas and Souflis 1984; Pitilakis and Moutsakis 1989; Collin 1992; Tateyama et al. 1995; Tatsuoka et al. 1996; Fang et al. 2003; Huang and Chen 2004; Trandafir et al. 2009). The main factors responsible for such damage are the increase of lateral earth pressure on walls, a possible phase shift between walls and backfill motions, and the accumulated tilt of the walls and its effect on the lateral earth pressure. Unfortunately, only a few case histories investigating the behavior of retaining walls under seismic loading are properly documented. Therefore, numerical analysis and theoretical approaches play key roles in understanding the dynamic response of retaining walls. However, studying the dynamic response of soil–retaining wall systems is a very challenging task. Some of the main factors contributing to the complexity of the model are soil nonlinear behavior that effects its stiffness, geometric variation and its effect on the fundamental frequencies of deposits, soil inhomogeneity in the form of spatial variations in properties, dynamic soil–wall interactions, and the dynamic characteristics of walls. A summary of previous analytical and numerical works concerning the dynamic response of soil–retaining wall systems and the objectives and scope of this study are provided in the following sections.

Previous Analytical Work

The seismic analysis of retaining walls can be broadly categorized into force-based methods and displacement-based methods. One of the most widely accepted force-based approaches is the Mononobe–Okabe (M–O) method developed by Okabe (1926) and Mononobe (1929). In this method, the effect of an earthquake is simulated by a pseudostatic acceleration acting on a Coulomb active or passive wedge. One of the main limitations of the M–O method is the inability to impart any information regarding the displacement of retaining walls. Another shortcoming of this method is that it does not account for wall flexibility and its possible rotation or sliding. To address these issues, displacement-based methods were developed as a new approach to the design of retaining walls based on allowable wall deformation. Newmark (1965) introduced a sliding block model to calculate the earthquake-induced permanent displacement of dams and embankments. Various techniques utilizing Newmark's sliding block method have been presented in recent decades (Richards and Elms 1979; Whitman and Liao 1985; Zeng and Steedman 2000; Trandafir et al. 2009; Caltabiano et al. 2012).

Newmark's sliding block method and its improved variations still suffer from an inability to effectively predict the seismic response of backfill, which affects dynamic soil thrust and earthquake-induced wall displacements (Nadim and Whitman 1983; Kramer and Smith 1997; Wartman et al. 2003; Trandafir et al. 2009). Additionally, both numerical and experimental studies have shown that Newmark's sliding block method is not able to properly describe the observed dynamic behavior of embedded sheetpile walls (Zeng 1990; Zeng and Steedman 1993; Callisto and Soccodato 2007;

[1]Graduate Research Assistant, Dept. of Civil and Environmental Engineering, Southern Methodist Univ., P.O. Box 750340, Dallas, TX 75275. Email: sfarzisizkow@smu.edu

[2]Associate Professor, Dept. of Civil and Environmental Engineering, Southern Methodist Univ., P.O. Box 750340, Dallas, TX 75275 (corresponding author). ORCID: https://orcid.org/0000-0003-1214-9040. Email: uelshamy@lyle.smu.edu

Note. This manuscript was submitted on October 30, 2019; approved on August 13, 2020; published online on November 19, 2020. Discussion period open until April 19, 2021; separate discussions must be submitted for individual papers. This paper is part of the ***Journal of Geotechnical and Geoenvironmental Engineering***, © ASCE, ISSN 1090-0241.

Conti et al. 2012). Conti et al. (2012) conducted centrifuge dynamic tests on cantilever retaining walls embedded in dry sand, and the results showed that the walls experienced much larger displacements compared to what was predicted using Newmark analysis. It was observed that the walls experienced significant displacement even before the critical acceleration was reached.

Previous Numerical Work

Owing to the complexity of the coupling relationship between soil and flexible retaining walls, numerical approaches, such as the finite-element method (FEM), are usually used to investigate the behavior of soil–retaining wall systems (Al-Homoud and Whitman 1990; Psarropoulos et al. 2005; Madabhushi and Zeng 2006; Al Atik and Sitar 2010; Cakir 2013; Gazetas et al. 2016; Osouli and Zamiran 2017; Lin et al. 2018; Bakr and Ahmad 2018; Ko and Yang 2019).

The discrete-element method (DEM) is a very powerful numerical technique for modeling discontinuous media such as soil and is gaining increasing popularity among geotechnical engineers. This method was originally developed by Cundall and Strack (1979) and has been widely used by various researchers (Zamani and El Shamy 2011; El Shamy and Aydin 2008; El Shamy and Zeghal 2005; Dobry and Ng 1992; Thornton 2000; Evans and Frost 2010; Radjaï and Dubois 2011; O'Sullivan 2011). The method has several advantages over other numerical techniques. Nonlinear soil behavior is inherently accounted for by the motion of particles and their rearrangement. This in turn leads to the creation and loss of some interparticle contacts and, possibly, sliding of particles. In addition, spatial variation in the properties of deposits is guaranteed by the random generation of particles.

The DEM has been used by various researchers to study various phenomena in connection with retaining walls. Chang and Chao (1994) used the DEM to investigate the active and passive earth pressure distribution that develops during different modes of wall movement. Nadukuru and Michalowski (2012) conducted DEM simulations to obtained earth pressure distributions on retaining walls considering the arching effect, and they computed the centroid of stress distribution for transitional and rotational wall movements. The plane-strain failure of dry-stone retaining walls was analyzed through two-dimensional (2D) DEM simulations by Oetomo et al. (2016), and the results were compared with the experimental data. Nadukuru and Michalowski (2012) examined the impact of dry granular flow in an inclined chute on a rigid wall. Nonspherical particles were used in the DEM simulations, and the effect of inclination angle was also investigated. Jiang et al. (2014) performed 2D DEM simulations to analyze the performance of cantilever retaining structures installed on lunar terrain. The previously mentioned studies are good examples showcasing the DEM's ability to handle problems pertaining to retaining structures. However, the dynamic response of soil–retaining wall systems, which requires more complicated problem setup and more sophisticated dynamic boundary conditions, was outside the scope of these studies.

Objectives and Scope

This study aims to assess the potential of the DEM to satisfactorily predict the dynamic behavior of soil-flexible retaining wall systems. This work serves as a proof of concept, and comprehensive parametric studies are needed and planned for future work. In this paper, a microscale model is presented to simulate the dynamic response of a sheetpile/granular backfill system using the DEM. The soil deposit is modeled as an assembly of spherical, rigid particles that can interact with each other through contact points. The sheetpile wall is created using small particles glued together by parallel bonds. The seismic load is introduced to the model by the base wall that represents the bedrock. Free-field boundaries are installed at both ends to avoid reflection of propagating waves into the assembly and apply the free-field motion. Free-field wave propagation in the elastic range was validated against theoretical expressions. The analytical method developed by Conti and Viggiani (2013) was employed to validate the simulation results.

Modeling Approach

Soil Deposit–Wall System

In this study, the dynamic behavior of soil–retaining wall systems is investigated using a microscale-based approach. The soil deposit is modeled as an assembly of spherical particles underlain by a rigid base. While it is almost impossible to replicate exact conditions inside a real soil deposit at the microscopic level, as a good approximation, the microscale properties of the DEM (e.g., interparticle friction, particle stiffness, and particle size distribution) can be adjusted in such a way that the macroscale behavior of the numerical model mimics that of a real deposit. To this end, the friction angle and maximum shear modulus of the DEM model is computed through numerical tests to make sure they are close to the corresponding values for the prototype deposit. In addition, the rolling resistance contact model is employed to avoid unrealistically large rotational movements of the particles and to account for the nonsphericity of real soil grains.

In numerical simulations using the DEM, it is computationally expensive to use particles with realistic soil grain shapes. Technological advances provide us with more computational power; however, it is still difficult to simulate real granular systems consisting of large numbers of particles without using some form of simplification. Therefore, particles are usually idealized as spherical bodies to avoid the complications caused by shape irregularity. The importance of rotational inertia on energy dissipation and shear strength of granular materials in quasi-static and dynamic regimes has been demonstrated by both numerical simulations and experimental studies (Bardet and Huang 1992; Bardet 1994; Iwashita and Oda 1998; Oda et al. 1982; Calvetti et al. 1997; Misra and Jiang 1997). The energy dissipation mechanisms may arise from different micromechanical processes in real granular systems, such as adhesion of the contact areas, surface roughness, and nonsphericity of particles (Itasca 2019). To account for the effects of particle shape on energy loss during rotational particle movements, the rolling resistance contact model was incorporated into DEM simulations by various researchers (Iwashita and Oda 1998; Oda et al. 1982; Calvetti et al. 1997; Misra and Jiang 1997).

The rolling resistance contact model used in this study is based on a linear contact model that incorporates a torque acting on contacting particles and resisting their rolling motions. The rolling resistance contact model behavior is similar to that of the linear contact model, except that relative rotation of contacting particles at the contact point produces an internal moment at the contact (Iwashita and Oda 1998). The retaining wall is modeled as a three-degree-of-freedom, flexible body composed of particles connected by parallel bonds to simulate the physical characteristics of a real-life cantilevered retaining wall. This type of bond acts in parallel with linear contact springs and are able to transmit both force and moment between the contacting particles. The overall flexibility of the wall can be controlled by adjusting the stiffness of the bonds (Zamani and El Shamy 2012).

Free-Field Boundaries

When a traveling wave reaches a fixed end boundary, it will be completely reflected and all of its wave energy will be trapped inside the medium. In contrast, in cases of an infinite medium or elastic boundary, all or part of the energy of the wave will be transmitted through the interface. Therefore, to simulate an infinite medium, different types of absorbing boundaries are developed to prevent the wave energy from being trapped inside the assembly. Lysmer and Kuhlemeyer (1969) and White et al. (1977) proposed a very popular absorbing boundary scheme utilizing dashpots attached independently to boundaries.

A simple type of absorbing boundary can be used without any modification when the only source of excitation is inside the model. However, it should not be used at the sides of the model when the seismic load is applied as a boundary condition at the base, because it distorts and attenuates the upward propagating wave (Itasca 2019). In this case, free-field boundaries must be utilized to absorb outgoing waves and account for the free-field motion existing at relatively large distances from the model.

The method described by Zienkiewicz et al. (1989) is used herein to implement free-field boundary conditions at the far left and right ends of the model. In this method, free-field columns with the same height as the soil deposit are defined on both sides and are connected to the lateral boundaries, with dashpots representing the acoustic impedance of the medium. The dashpots only apply forces to the boundaries of the main model; the responses of the free-field columns are not affected. These forces are proportional to the relative velocities between boundaries and free-field columns.

To implement free-field boundaries, a number of steps were taken: (1) a dynamic load was applied to the free-field columns in advance, and the average velocities at different heights were recorded; (2) fixed conditions were removed at both ends of the main model; (3) supporting forces, equal to static reaction forces, were applied to boundary particles; and (4) dashpots were attached to these particles that act on the difference between free-field and boundary motions. The imposed normal stress applied by the dashpot on particle i is

$$\sigma_i = v_p \rho (\dot{u}^{ff} - \dot{u}_i^m) \tag{1}$$

where v_p = p-wave velocity; ρ = average density of the assembly of particles; $\dot{u}_i^m$ = normal component of the velocity for boundary particle i; and $\dot{u}^{ff}$ = normal component of the free-field velocity for a point located at the same level as particle i. It is very difficult to determine the exact values for the p-wave velocity and average density of the assembly. Therefore, to obtain the discrete equivalent form of this equation, several calibration runs must be performed on an assembly with similar particle packing and micro properties. The forces created in the dashpot associated with particle i can be calculated using the following equation:

$$F_i^d = \beta D^2 v_p \rho (\dot{u}^{ff} - \dot{u}_i^m) \tag{2}$$

in which F_i^d = damping force on particle i; D = particle diameter; and β = coefficient that adjusts the acoustic impedance.

Computational Scheme

PFC3D software version 6.0 (Itasca 2019) was used to perform the DEM analysis presented in this study. The soil–sheetpile interaction was done in a fully coupled scheme in the time domain. PFC3D uses an explicit central finite difference algorithm to solve the equations of motion at each time step. The stiffness and damping coefficients of the interparticle contacts as well as the mass of the particles govern the critical time step needed to conduct a stable simulation. The contact forces and moments at each time step are used to obtain the particle positions for the next time step.

Table 1. Scaling laws for conducted simulations ($N = g$-level multiplier)

Parameter	Model/prototype
Gravity	N
Length	$1/N$
Acceleration	N
Velocity	1
Density	1
Mass	$1/N^3$
Strain	1
Stress, pressure	1
Flexural rigidity	$1/N^4$
Force	$1/N^2$
Moment	$1/N^3$
Time	$1/N$

Model Description

The proposed approach was used to investigate the response of a three-degree-of-freedom flexible wall retaining a dry granular backfill. To reduce the domain size and simulation time, the high g-level concept was exploited (Iai et al. 2005). In this study a gravitational field of 50 g is used and scaling laws are applied to obtain the model dimensions (Table 1). Based on the nature of the problem, only a thin slice of the domain was modeled. This setup yields an overall behavior of the system that is similar to a 2D plane-strain problem in continuum-based models. Periodic boundaries were installed at the front and back sides of the model to simulate an infinitely repeated system in the lateral direction and to avoid the reflection of propagating waves.

The heights of the soil deposit in front of and behind the retaining wall were, respectively, 12 and 18 cm (6 and 9 m in prototype units). The location of the right and left end boundaries were selected far enough (40 cm behind the wall and 14 cm in front of the wall in model units) to allow for full development of the failure wedges behind and in front of the wall. The soil deposit has a thickness of 3 cm (1.5 m in prototype units) and average porosity of 0.4. Soil particles constituting the deposit are between 1.5 and 2.5 mm and have a density of 2,650 kg/m^3.

The flexible retaining wall had a free height of 6 cm (3 m in prototype units). The friction angle of the dry soil deposit was needed to determine the penetration depth of the sheetpile. Therefore, separate consolidated drained DEM triaxial tests were conducted on a similar packing density of the deposit particles to estimate the friction angle of the soil. According to those simulations, the φ-angle of the idealized soil was about 31°. The theoretical static active and passive coefficients of lateral earth pressure were calculated from the soil friction angle. A lateral pressure distribution diagram was obtained, and the depth of embedment needed for the stability of the wall was calculated. After obtaining the theoretical depth of penetration, the actual depth was increased by 30%. The total calculated length of the wall was 13.5 cm (6.75 m in prototype units) and the sheetpile was assigned an assumed thickness of 5 mm (25 cm in prototype units).

The sheetpile was modeled by two sheets of particles with a size of 2.5 mm (total thickness of 5 mm). These particles were glued together using parallel bonds that could transmit both force and moment (Zamani and El Shamy 2012). The density of the concrete

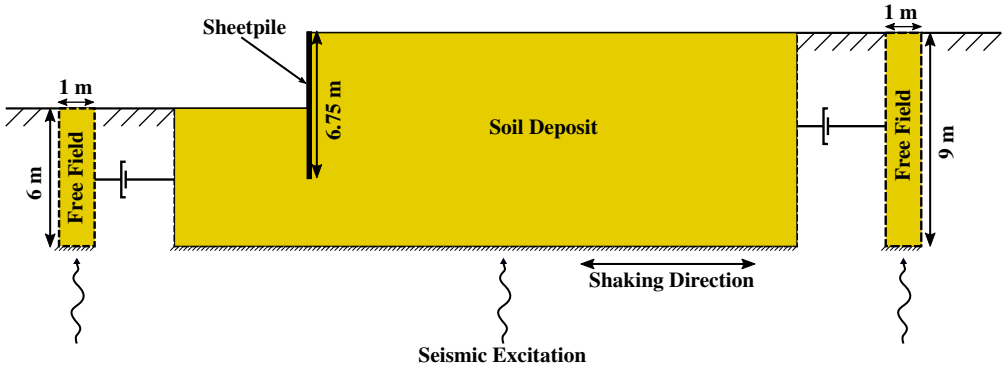

Fig. 1. Schematic configuration of soil-retaining wall system.

retaining wall was assumed to be 2,400 kg/m^3, which resulted in each particle composing the wall to have a density of 4,000 kg/m^3 in order for the model and the prototype to have equal masses. The total mass of the retaining wall was determined to be 0.042 kg (5,300 kg in prototype units). The stiffness of the bonds was determined in such a way that the modeled wall mimicked the behavior of a concrete sheetpile with a Young's modulus of 40 GPa. That is, a series of calibrating DEM tests were performed on the sheetpile by fixing one end and applying a vertical load to its free end. The bond stiffness was fine-tuned so that the deflection of sheetpile almost perfectly matched the value obtained from the analytical solution for a concrete cantilever beam with the same dimensions. The flexural stiffness of the sheetpile was determined to be 11.6×10^6 N · m/rad in prototype units. In addition, direct shear tests were conducted to determine the right coefficient of friction for sheetpile particles to produce an angle of friction between the wall and soil equal to half the soil friction angle.

A schematic model of the sheetpile/soil deposit system along with free-field boundaries is presented in Fig. 1. The two end boundaries and the base of the deposit were initially modeled as rigid walls. Particles needed for creating a soil deposit with a height of 12 cm (the dredge level) were generated at a larger space and allowed to settle under the high gravitational field of 50 g. To install the sheetpile, first, the part of the soil deposit occupying the embedded length of the wall was removed. Then the particles composing the sheetpile were created at the specified locations, and parallel bonds were installed between them. The wall was fixed in all directions during this stage, so that the surrounding soil particles could rearrange themselves and enough contacts with the sheetpile were created. Once the model reached equilibrium, the fixity of the sheetpile in the vertical direction was removed and the wall underwent very slight settlement until the forces acting on it became balanced. Then the rotational and horizontal fixities of the wall were removed, and more loose particles were added behind the wall to reach the desired backfill height of 18 cm (9 m in prototype units). The wall experienced some rotation during this stage, and the system reached its final static equilibrium. The final dry assembly of particles consisted of more than 350,000 particles with an average porosity of 0.4 and average density of 1,600 kg/m^3. A summary of simulation details and the soil deposit properties are provided in Tables 2 and 3, respectively. The information pertaining to the space and time dimensions as well as the results is presented hereafter in prototype units unless otherwise specified.

At the last stage, the free-field boundaries were installed at the right and left sides of the model. Implementation of the free-field boundaries was carried out in the following steps. First, two free-field columns with periodic lateral boundaries were created. These columns had the same height as the soil deposit in front of and behind the wall and a width of 1 m. Then, through two separate DEM simulations, the dynamic load (the same ground acceleration later introduced into the main model during the main simulation) was applied to the free-field columns, and the time histories of the average horizontal velocities inside the measurement spheres located at different heights of the free-field columns were recorded. Then the particles touching the two end boundary walls of the main model were detected. Next, the boundary walls were removed from the main deposit, and supporting static forces were applied to the boundary particles equal to the original static reaction forces. Finally, dashpots were attached to the boundary particles that represent the acoustic impedance of the medium acting on the difference between the horizontal velocities of the boundary particles

Table 2. Simulation details in model units

Parameter	Value
Soil deposit	
Diameter (mm)	1.5–2.5
Normal stiffness (N/m)	5.0×10^5
Shear stiffness (N/m)	5.0×10^5
Normal critical damping ratio	0.1
Shear critical damping ratio	0.0
Friction coefficient	0.5
Rolling friction coefficient	0.2
Density (kg/m^3)	2,650
Number of particles	359,879
Computation parameters	
g-level	50
Time step for DEM (s)	1.2×10^{-7}
Sheetpile properties	
Thickness (mm)	5
Width (mm)	30
Height (mm)	135
Mass (kg)	0.042
Particle diameter (mm)	2.5
Parallel bond stiffness (N/m^3)	2.16×10^{13}

Table 3. Soil deposit properties in prototype units

Parameter	Value
Dry unit weight (kN/m^3)	16
Porosity	0.4
Void ratio	0.67
Angle of internal friction (°)	31
Fundamental frequency (Hz)	5.8–8.75
Low strain shear wave velocity (m/s)	210
Low strain shear modulus (MPa)	70

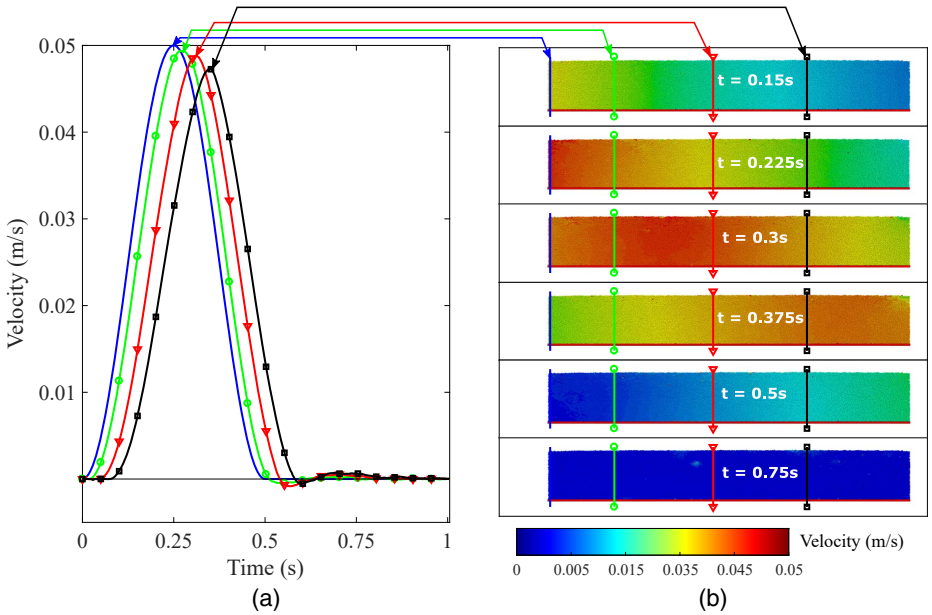

Fig. 2. (a) Average particle velocities versus time on four different planes; and (b) particle velocity contours at different time instances.

during the main simulation and the velocities obtained from free-field column simulations at the same height and time instant.

To investigate the performance of the absorbing dashpots, a separate soil deposit was created with the same particle size distribution and porosity as the main model. Then the absorbing dashpots were installed at the right end boundary following the same steps mentioned earlier and an impulse wave was injected into the assembly of particles from the left end boundary. The dashpots in this simulation only absorb the traveling wave energy, and there is no free-field motion to impose in this case. The velocity contours and the average particle velocities during the simulation at four different planes, shown by colored lines, are presented in Fig. 2. It can be seen that the injected wave travels through the soil deposit and crosses the right end boundary with almost no reflection. The proper value of β in Eq. (2) was determined to be about 1.3 after a number of calibration runs.

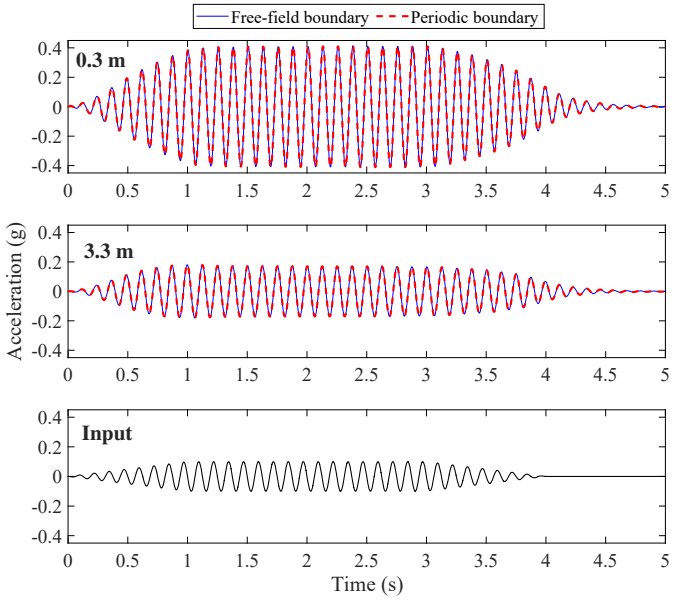

Fig. 3. Comparison of acceleration time histories recorded for deposits with periodic and free-field boundaries.

Additional DEM simulations were carried out to see how the free-field boundaries affected the upward propagating wave. Two soil deposits were created with a height and width of, respectively, 6 and 2 m resting on a rigid base wall. The deposits had the same particle size distribution and properties as the main model. A no-slip boundary condition was also specified at the base. The first model had periodic boundaries at the sides, while free-field boundaries were installed for the second model. The deposits were excited from the base by a sinusoidal wave with a maximum amplitude of 0.1 g, frequency of 8 Hz (which is close to the natural frequency of the deposits) and a total duration of 5 s. Fig. 3 shows a comparison between the accelerations obtained during the two simulations at two different points located at depths of 0.3 and 3.3 m. It can be seen that the results are almost identical for the two simulations. The results confirm that the implemented free-field boundaries do not attenuate or distort the propagating wave.

Fig. 4 shows the final DEM model of the sheetpile/soil deposit system. The described soil–retaining wall system was used in all subsequent simulations. The system was subjected to two types of dynamic excitations applied to the bedrock (base wall), and the responses of soil deposit and retaining wall were monitored. The first type of dynamic excitation followed a sinusoidal pattern with a total duration of 8 s. The amplitude of the input motion gradually increased to reach its maximum value (a_g) during the first 3 s, then it remained constant for the next 4 s, and it gradually vanished during the last second. A range of input motion amplitudes and frequencies were selected to analyze their influence on the dynamic response of the system. The weak input acceleration amplitude of 0.01 g represents a seismic event during which no significant deformation is expected in the system. Therefore, it can reveal essential information regarding the natural frequency, low strain shear wave velocity, and shear modulus of the deposit. The input motions with the amplitude of 0.1 g simulate seismic events of moderate strength and were expected to induce some

J. Geotech. Geoenviron. Eng., 2021, 147(2): 04020157

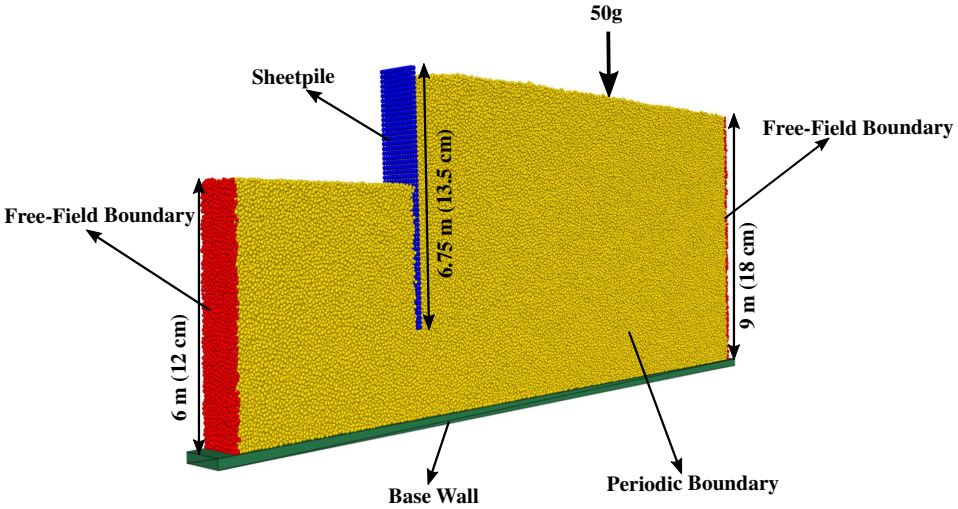

Fig. 4. Granular deposit and retaining wall structure as modeled in DEM simulations.

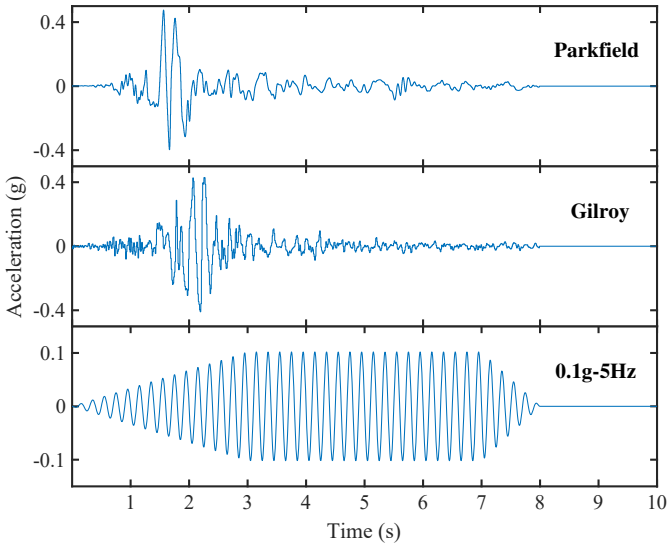

Fig. 5. Scaled Gilroy and Parkfield and 0.1*g*-5 Hz input motion time histories.

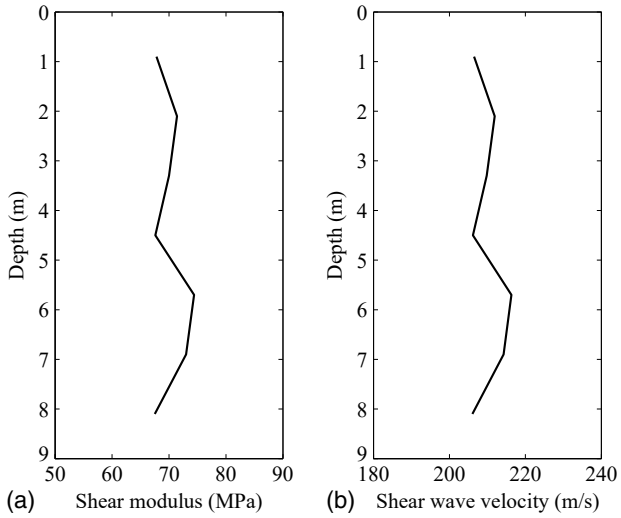

Fig. 6. (a) Low strain shear modulus profile; and (b) shear wave velocity profile.

deformation without causing catastrophic failure. An amplitude of 0.3 g represents a severe seismic excitation wherein there exists the possibility of complete failure of the system.

Modified versions of actual recorded ground motions during real earthquakes were used as the second type of dynamic excitation in this study. The records of the Gilroy, California, October 17, 1989, and Parkfield, California, June 28, 1966, earthquakes were scaled in a way that they had, respectively, dominant frequencies of 5 and 4 Hz, a maximum amplitude of about 0.4 and 0.5 g, and a total duration of 8 s. Scaled Gilroy and Parkfield ground motions along with 0.1*g*-5 Hz excitation are presented in Fig. 5.

Characteristics of Soil–Sheetpile System

Backfill

As mentioned earlier, the simulations with a maximum acceleration amplitude of input motion of 0.01 g were used to compute the dynamic properties of the backfill. The shear strains inside the soil deposit induced by this low acceleration amplitude are very small and considered to be at a nondestructive level. Therefore, this will provide important information regarding the average maximum shear modulus and low strain shear wave velocity of the deposit. The low strain shear moduli and shear wave velocities along the depth of the deposit were obtained and plotted in Fig. 6. This figure shows that the shear modulus and shear wave velocity have fairly constant values throughout the deposit. The average value for the low strain shear modulus was determined to be approximately 70 MPa. The corresponding average low strain shear wave velocity and the fundamental frequency of the backfill were about 210 m/s and 5.8 Hz, respectively. The shear strains that develop during simulations with the input motion amplitudes of 0.1 and 0.3 g can result in soil softening, degradation of the shear modulus, and, consequently, reduction of the fundamental frequency of the deposit. For example, the average shear modulus dropped to around 50 MPa during the 0.1-g simulation, which corresponds to a shear wave velocity of 175 m/s and a natural frequency of about 4.9 Hz.

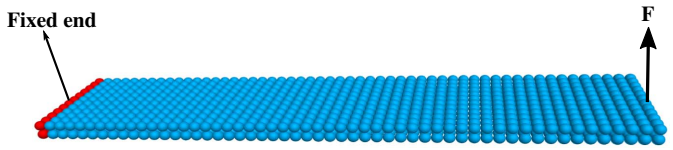

Fig. 7. DEM model of sheetpile.

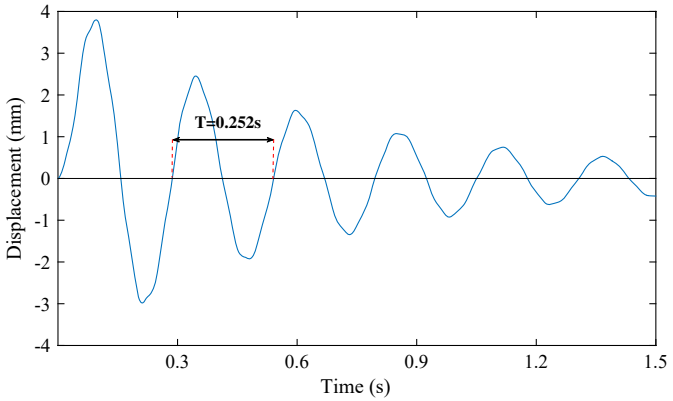

Fig. 8. Dynamic displacement at top of sheetpile versus time.

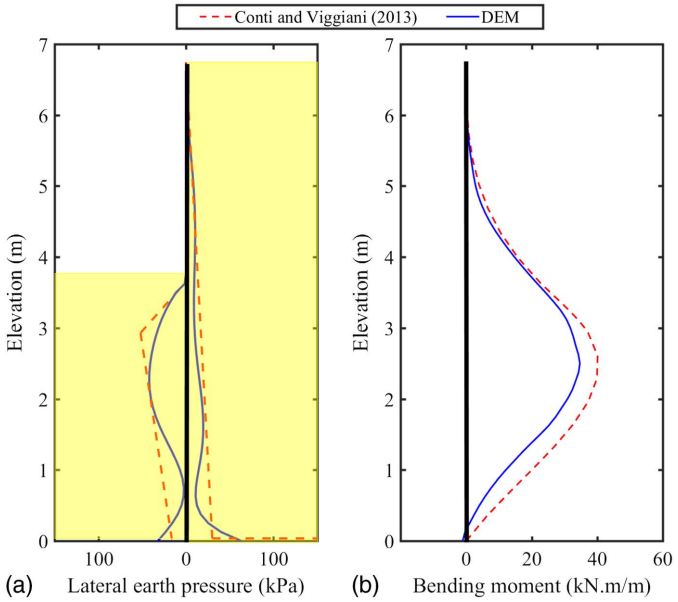

Fig. 9. Comparison of results of DEM simulation and analytical method: (a) initial lateral earth pressure; and (b) initial bending moment.

Sheetpile

Theoretical and numerical approaches were used to obtain the fundamental frequency of the sheetpile. The characteristic equation of a cantilever Euler–Bernoulli beam is (Chopra 2017)

$$\cos \lambda l \times \cosh \lambda l = -1 \tag{3}$$

where l = length of cantilever beam; and λ is defined by

$$\lambda = \left(\frac{4\pi^2 f^2 \rho A}{EI}\right)^{\frac{1}{4}} \tag{4}$$

where E = Young's modulus; I = moment of inertia; ρ = density; A = cross-sectional area; and f = natural frequency of cantilever beam. As a first approximation, the sheetpile was assumed to be fixed at its toe. Thus, the first fundamental frequency of the sheetpile can be calculated as

$$f_1 = \frac{1}{2\pi}\left(\frac{EI\lambda^4}{\rho A}\right)^{\frac{1}{2}} = 4.01 \text{ Hz} \tag{5}$$

A DEM simulation was also performed to confirm the analytical result. In this test, the previously described sheetpile (Fig. 7) was completely fixed at the left end, and a vertical load was applied to its free end to create a small deflection. The load was then removed, and the free oscillation of the cantilever wall was monitored. Fig. 8 shows the dynamic displacement at the tip of the wall as a function of time. The numerical simulation shows that the natural period and frequency of the sheetpile are, respectively, 0.252 s and 3.96 Hz, consistent with the results of the theoretical calculations. In addition, the local damping coefficient of the sheetpile particles was selected to be 0.12, which resulted in an overall damping coefficient of 5% for the wall structure. Based on the initial natural frequencies of the backfill and sheetpile and the expectation that the natural frequency of the deposit would decrease during simulations with larger amplitudes of input motion, the frequency (f) of the input motions was selected to be between 1 and 6 Hz.

Static Lateral Earth Pressure

The M–O method has been used frequently to estimate the total soil thrust on retaining walls during earthquakes. However, it is only applicable when each side of a wall is subjected to pure active or passive earth pressures, which is not the case for cantilever retaining walls. Therefore, the analytical method presented by Conti and Viggiani (2013) was used in this study to validate the numerical simulation results for the lateral earth pressure distribution on the wall. Initial lateral earth pressure distributions on the front and back of the retaining wall obtained by DEM simulation and analytical approach are shown in Fig. 9(a). In the method proposed by Conti and Viggiani (2013), on the backfill side, the soil is in active and passive states above and below the pivot point, respectively. However, on the excavated side, the full passive strength of the soil is mobilized only down to a point ($\bar{d}$), and the soil is in an active state below the rotation point. The lateral earth pressure changes linearly between $\bar{d}$ and the pivot point. The active and passive earth pressure coefficients are calculated using (Lancellotta 2002, 2007) closed-form solutions. The force and moment equilibrium equations are solved to obtain the pivot point and depth $\bar{d}$.

It can be observed from Fig. 9(a) that the numerical and analytical results show a similar pattern for the initial static lateral earth pressure on both sides of the sheetpile. The earth pressure behind the wall is in an active state down to near the bottom of the wall and increases significantly below the pivot point as it becomes a passive state. In front of the wall, the lateral earth pressure increases with a sharp slope down to a point and then decreases to the active limit state. Fig. 9(b) shows the initial static bending moment over the length of the sheetpile obtained by DEM simulation and the analytical method. It can be seen that the maximum bending moment is located at the same depth, and the two results show a fair agreement. However, the analytical method predicts a higher maximum bending moment compared to the numerical solution (40 kN · m/m compared to 34.73 kN · m/m).

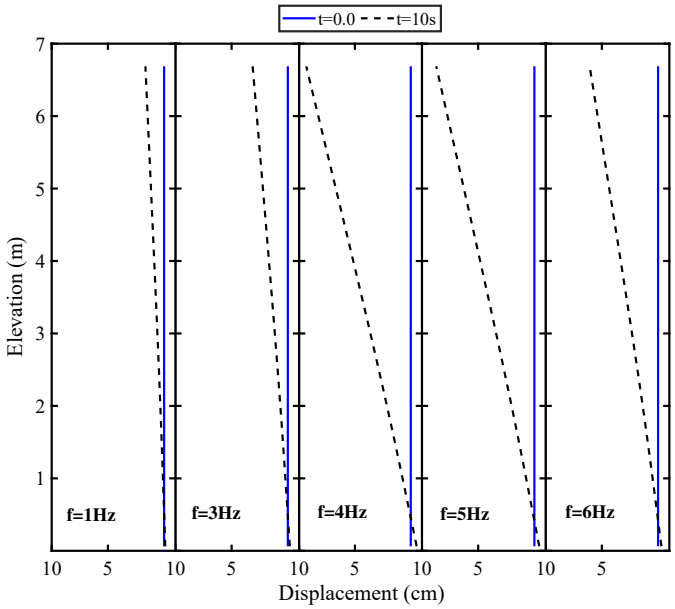

Fig. 10. Sheetpile deformed shape ($a_g = 0.1g$).

Simulation Results

A total of 11 seismic load combinations of input motion magnitude and frequency were investigated in this study. The following sections present an in-depth analysis of the simulations with the input motions with a maximum amplitude of 0.1 g and an overview of key results from the remaining simulations. Choosing this input motion was based on the fact that it represents a seismic event of moderate severity that is unlikely to cause significant failure, which further complicates the analysis. In addition, two actual earthquake records were customized to produce ground accelerations with dominant frequencies of 5 and 4 Hz, maximum amplitudes of about 0.4 and 0.5 g, and a total duration of approximately 8 s. These ground motions were introduced into the model, and the dynamic response of the system was monitored. The results obtained from these simulations are discussed in what follows.

Flexible Retaining Wall Response

Displacement

Earthquake-induced displacement is one of the most important factors in the seismic design of cantilever retaining walls. According to the Newmark (1965) method, which is very popular for calculating the permanent displacements of retaining walls, for accelerations smaller than the critical acceleration of the wall there will be no permanent wall displacements. However, previous studies of the dynamic response of the cantilever retaining walls showed that a wall can experience significant permanent displacement even before the critical acceleration is reached (Zeng 1990; Zeng and Steedman 1993). This displacement can lead to a considerable increase in the internal forces in a retaining wall (Conti and Viggiani 2013). In the absence of reliable analytical solutions, numerical simulation is a powerful tool for evaluating and predicting the seismic displacements of flexible retaining walls.

Horizontal displacements of sheetpile particles at different elevations were monitored during the DEM simulations, and the final position of the sheetpile was obtained. Fig. 10 shows the deformed shape of the wall for the seismic excitation with a maximum amplitude of 0.1 g and frequencies of 1–6 Hz. It is evident from Fig. 10 that the displacements of the sheetpile are mostly rigid rotations, and the pivot point is located near the bottom of the wall. This can be due to the relatively high rigidity of the sheetpile compared to soil. As mentioned earlier, at this excitation amplitude some degradation of shear modulus and, consequently, a shift in the natural frequency of the backfill were expected. The results show that the maximum wall displacement corresponds to the input motion with frequencies of 4 and 5 Hz, which are close to the natural frequencies of the sheetpile and backfill, respectively. The sheetpile experienced maximum displacements of roughly 9.3 and 8.7 cm for input motion frequencies of 4 and 5 Hz, respectively. The input acceleration with a frequency of 1 Hz induced the smallest displacement in the sheetpile, which was less than 2 cm at the top. It is worth noting that input motion with a frequency close to the fundamental frequency of the sheetpile (4 Hz) induced a larger deformation in the sheetpile than that of backfill (5 Hz). The displacement at the top of the sheetpile as a function of time for different frequencies is presented in Fig. 11. It shows that the sheetpile oscillates at the same frequency as the input acceleration, and the net displacement increases during the dynamic loading until it reaches the final value. The same pattern was observed in the results obtained from experimental studies conducted by other researchers (Finn et al. 1992; Madabhushi and Zeng 2006).

For the maximum amplitude motion of 0.3 g, which represents severe seismic excitation, the fundamental frequency of the backfill further reduced to approximately 4 Hz. Fig. 12(a) shows the dynamic displacements of the sheetpile for this seismic excitation amplitude with frequencies of 1 and 4 Hz. It can be observed that even at the input motion frequency of 1 Hz, the sheetpile undergoes a maximum displacement of more than 12 cm. At the frequency of 4 Hz, which is the fundamental frequency of both sheetpile and backfill, the wall suffers a large rotation and maximum displacement of more than 27 cm. Fig. 12(b) shows the dynamic displacements of the sheetpile for the scaled versions of the Gilroy and Parkfield earthquakes. It can be seen that the sheetpile experiences a larger deformation at the top for the Parkfield earthquake compared to the Gilroy earthquake (9.5 cm compared to 8.8 cm).

To investigate the possible separation between the sheetpile and backfill during seismic loading, the phase differences between the accelerations at two points at the same level close to the ground

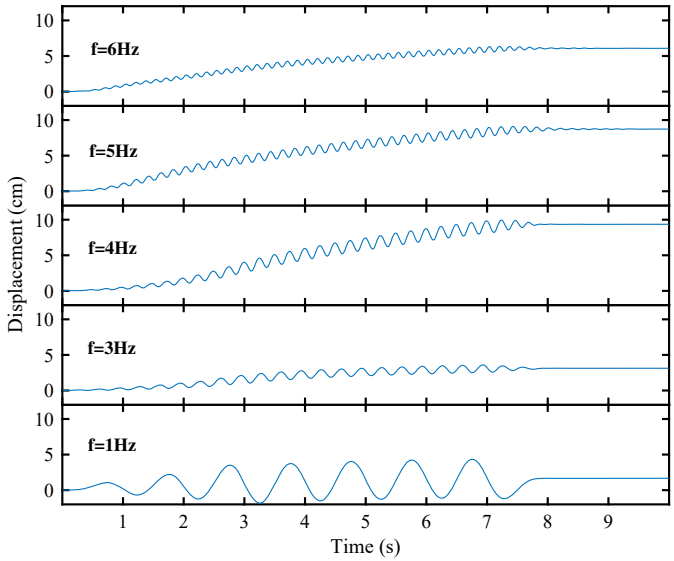

Fig. 11. Displacement at the sheetpile top versus time ($a_g = 0.1g$).

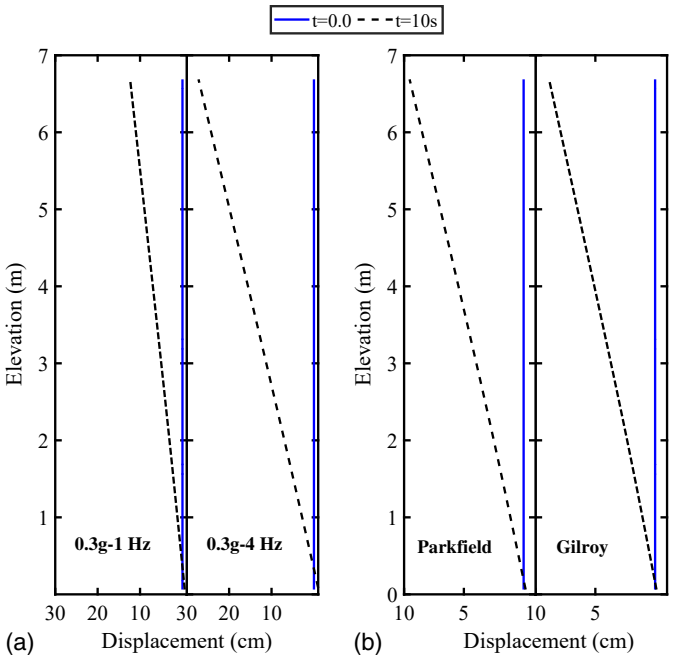

Fig. 12. Deformed shape of the sheetpile wall: (a) $a_g = 0.3g$; and (b) scaled earthquakes records.

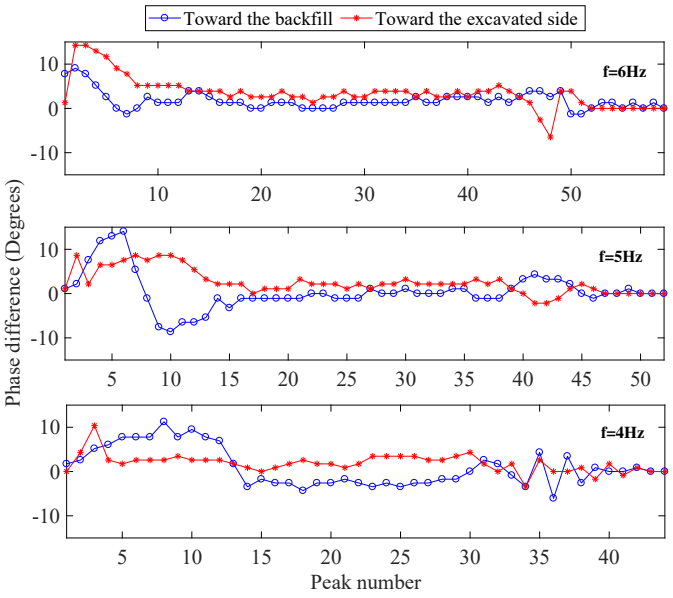

Fig. 13. Phase difference at different acceleration peaks ($a_g = 0.1g$).

surface, one on the sheetpile and one immediately behind it, were obtained. Fig. 13 shows the phase differences at all acceleration peaks in directions toward and away from the backfill for the simulations with maximum input acceleration of $0.1g$. The results show that the phase differences between the motions of the backfill and sheetpile are relatively small (less than 15°), and therefore, they are not expected to have a significant effect on the lateral earth pressure during seismic loading.

Soil Thrust and Lateral Earth Pressure

To obtain the lateral earth pressure distribution on both sides of the retaining wall, the contact forces acting on the particles composing

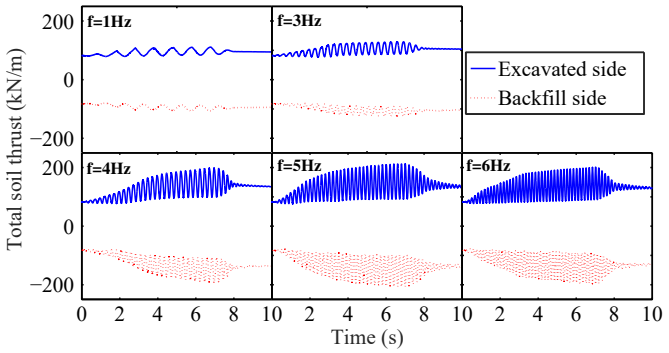

Fig. 14. Time histories of total soil thrust ($a_g = 0.1g$).

the sheetpile were tracked, and the sum of horizontal forces at each elevation was divided by the corresponding areas. The data were collected at a regular time interval during the simulation to investigate the dynamic and residual lateral earth pressures. Furthermore, the total soil thrusts were computed by summing all existing forces on each side of the sheetpile. Fig. 14 shows the total soil thrust on both sides of the sheetpile during seismic loading with a maximum amplitude of 0.1 g. It can be seen that the total active soil thrust behind the sheetpile increases during dynamic loading owing to the acceleration of the retained soil. In addition, the total passive and active soil thrusts in front of and behind the sheetpile remain equal and in opposite directions during the simulations, and the maximum soil thrusts for the input motion frequencies of 4, 5, and 6 Hz are close to 200 kN/m, which is approximately 2.5 times the initial static thrust. At input motion frequencies of 1 and 3 Hz, the maximum dynamic soil thrusts are, respectively, only 35% and 57% higher than the initial value. In addition, the residual soil thrusts for the input motion frequencies of 4–6 Hz have approximately the same value of about 135 kN/m, which is 65% higher than the initial static thrust. However, in the case of input motion frequencies of 1 and 3 Hz, the increases in the soil thrust are, respectively, only about 15% and 27% by the end of the simulations.

Fig. 15 shows the initial static, maximum dynamic, and residual lateral earth pressure distributions on both sides of the sheetpile at a seismic excitation amplitude of 0.1 g and frequencies between 1 and 6 Hz. The results show that the lateral earth pressure on the excavated side significantly increases during dynamic loading, especially at input motion frequencies of 4–6 Hz, which have similar maximum dynamic and residual earth pressures. In these cases, the maximum values of the dynamic and residual passive earth pressures in front of the retaining wall are approximately 2.5 and 1.95 times larger than the initial static earth pressure. However, at input motion frequencies of 1 and 3 Hz, the maximum dynamic and residual passive earth pressures are significantly smaller.

To further study the increase in the passive earth pressure on the excavated side of the sheetpile, the coefficient of earth pressure at a point located 1.5 m below the dredge level in front of the wall was monitored during the simulations. The changes in the coefficient of earth pressure at this point as a function of time at the input motion amplitude of 0.1 g are illustrated in Fig. 16. It can be seen that at input motion frequencies of 4, 5, and 6 Hz, there is a large increase in this coefficient by the end of the simulations. Fig. 17 shows the dynamic and average coefficients of earth pressure at this point versus wall rotation at input motion frequencies of 3–6 Hz. It is evident from Fig. 17 that the average coefficient of earth pressure increases as the wall rotates during the dynamic loading and reaches its maximum between 0.8% and 1% rotation, and after that it becomes relatively constant. The wall rotation is not recoverable,

J. Geotech. Geoenviron. Eng., 2021, 147(2): 04020157

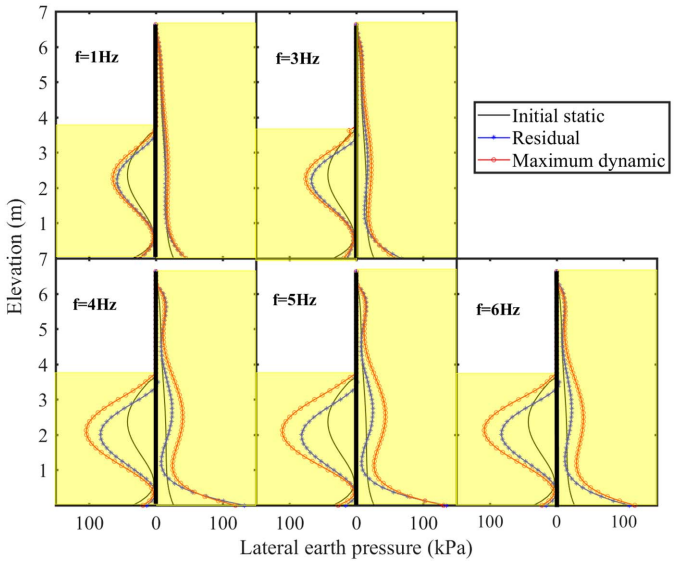

Fig. 15. Lateral earth pressure distribution along both sides of the sheetpile ($a_g = 0.1g$).

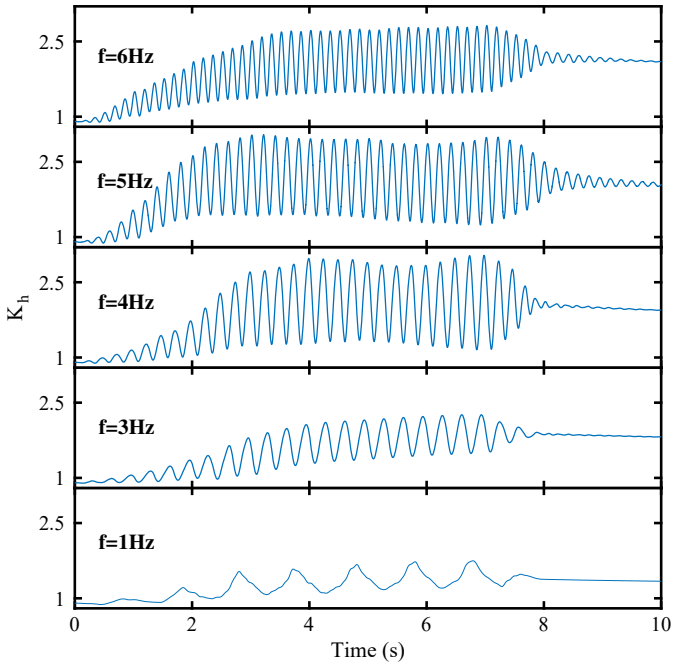

Fig. 16. Coefficient of earth pressure versus time ($a_g = 0.1g$).

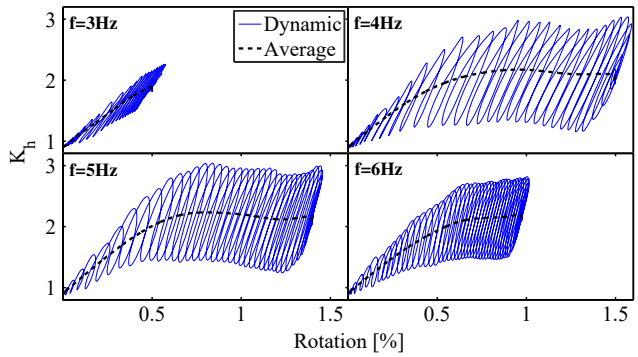

Fig. 17. Coefficient of earth pressure versus wall rotation ($a_g = 0.1g$).

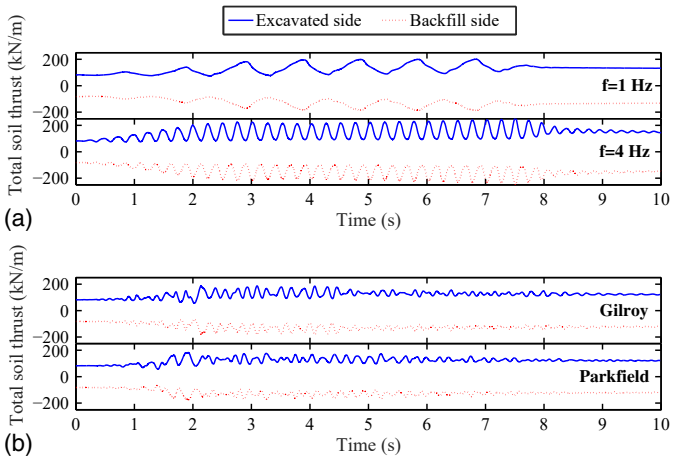

Fig. 18. Total soil thrust time histories: (a) $a_g = 0.3g$; and (b) scaled earthquakes.

so the coefficient of earth pressure at this point has a much higher final value. This leads to having considerably higher residual and dynamic passive earth pressures in front of the wall. It can be observed that during simulations at input frequencies of 4, 5, and 6 Hz, the wall undergoes enough rotation to activate the full passive strength of the soil down to 1.5 m below the dredge line on the excavated side. However, input motion frequencies of 1 and 3 Hz do not produce enough wall rotation to mobilize the full passive strength at this point.

Fig. 18(a) shows the total soil thrust as a function of time on both sides of the sheetpile during seismic loading with maximum amplitude of 0.3 g. It is observed that the maximum and residual soil thrusts for 0.3g-1 Hz input motion are close to what was obtained during 0.1-g simulations at frequencies of 4–6 Hz. However, the maximum and residual soil thrusts during the 0.3g-4 Hz simulation are larger than the maximum values obtained for 0.1 g simulations. The evolution of total soil thrust during the scaled earthquake motions are presented in Fig. 18(b). The results show a slightly lower maximum and residual soil thrusts compared to 0.1-g simulations at frequencies of 4–6 Hz.

The initial static, maximum dynamic, and residual lateral earth pressures on both sides of the sheetpile at a seismic excitation amplitude of 0.3 g and scaled earthquake motions are shown in Fig. 19. There is no significant difference when the results are compared to the lateral earth pressure distributions obtained for 0.1-g simulations at frequencies of 4–6 Hz.

The critical acceleration computed using the analytical method by Conti and Viggiani (2013) is approximately 0.36 g. This method proposes that if the surface acceleration exceeds this limit, the full passive strength of the soil in front of the sheetpile will be mobilized and the wall will rotate with constant internal forces. Fig. 20 shows the acceleration in the backfill immediately behind the sheetpile. It is evident that the maximum surface accelerations for all input motions except 0.1g-1 Hz and 0.1g-3 Hz surpass the critical acceleration. The results of the DEM simulations (Figs. 15 and 19) show that the maximum dynamic lateral earth pressure jumps from 75 kPa for the input motion of 0.1g-3 Hz (maximum acceleration

J. Geotech. Geoenviron. Eng., 2021, 147(2): 04020157

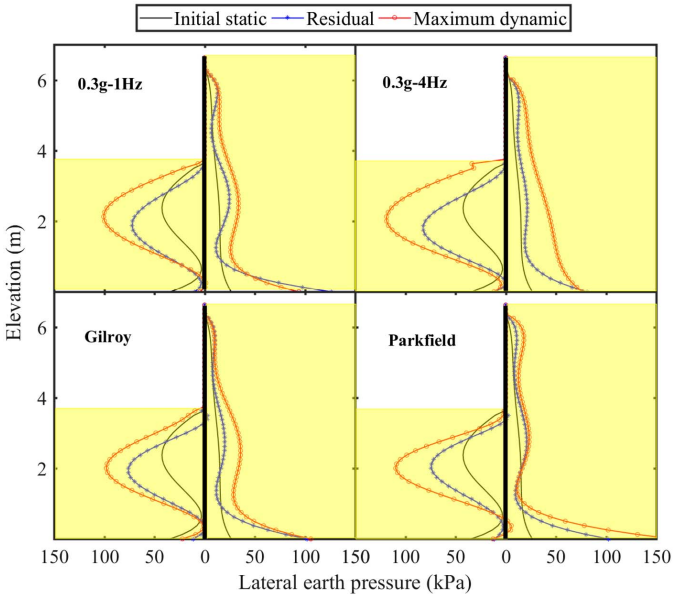

Fig. 19. Lateral earth pressure versus elevation for $a_g = 0.3g$ and scaled earthquakes.

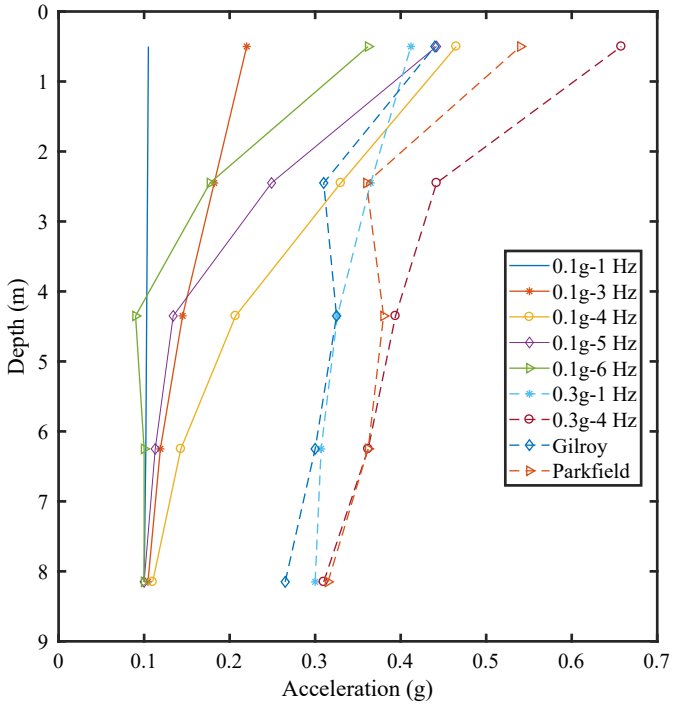

Fig. 20. Acceleration profiles in soil immediately behind sheetpile.

of 0.22g behind the wall) to 110 kPa for the input motion of 0.1g-6 Hz (maximum acceleration of 0.36g behind the wall). For stronger accelerations, the changes in the maximum lateral earth pressure are relatively small and the maximum dynamic lateral earth pressure is 118 kPa for the input motion of 0.3g-4 Hz (maximum acceleration of 0.65g behind the wall). However, the results clearly show that the critical state was never reached (meaning the full mobilization of the passive strength of the soil down to the pivot point in front of the wall) even for 0.3g-4 Hz case.

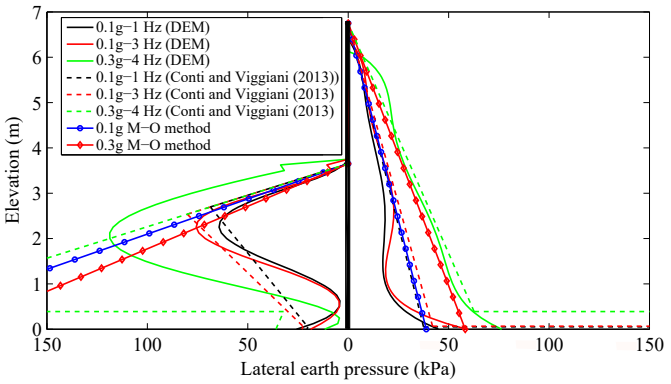

Fig. 21. Lateral earth pressure obtained from DEM simulation and analytical solutions.

The results suggest that the full passive strength of the soil is mobilized only down to approximately half the embedded part of the sheetpile.

The maximum dynamic lateral earth pressures obtained from the Conti and Viggiani (2013) method, the M–O method, and the DEM numerical simulations for the input accelerations of 0.1g-1 Hz, 0.1g-3 Hz, and 0.3g-4 Hz are shown in Fig. 21. The backfill side shows good agreement between these techniques and the DEM results in the active state region extending down to the pivot point. The DEM results show that in a small region below the pivot point the soil state changes to passive. The method proposed by Conti and Viggiani (2013) also demonstrates a similar pattern, though it predicts much larger passive pressures compared to the DEM. The M–O method does not account for the wall rotation and its effects; therefore, it considers that only an active state exists in the backfill. At the excavated side, the results of the three methods seem fairly consistent at the upper parts, where the soil is in a passive state. The DEM results and Conti and Viggiani's (2013) solution show that the lateral earth pressure gradually decreases until the soil state changes to active at the pivot point. The discrepancy between the results of the DEM and the Conti and Viggiani (2013) method is considerably larger for the input motion of 0.3g-4 Hz. According to the Conti and Viggiani (2013) method, this input motion is strong enough to mobilize the passive strength of the soil at the excavated side down to the pivot point. This is not consistent with the DEM results, where the lateral earth pressure increases only down to less than 2 m below the dredge line. The M–O method, as expected, fails to capture this transition from passive to active state.

Bending Moment

The maximum dynamic and residual bending moments induced by dynamic loading play crucial roles in designing cantilever retaining walls. Previous studies have shown that the bending moment can significantly increase during earthquakes and reach a final residual value substantially larger than the initial static moment (Madabhushi and Zeng 2006, 2007; Zeng 1990). In this study, the bending moments developed inside the parallel bonds connecting the sheetpile particles during the simulations were tracked. The distribution of bending moments on the wall during dynamic loading was obtained by summing up the parallel bond moments at the same height from the toe of the sheetpile.

Fig. 22 shows the initial static, maximum dynamic, and residual bending moments over the length of the sheetpile at a seismic excitation amplitude of 0.1 g and frequencies of 1–6 Hz. Note that the

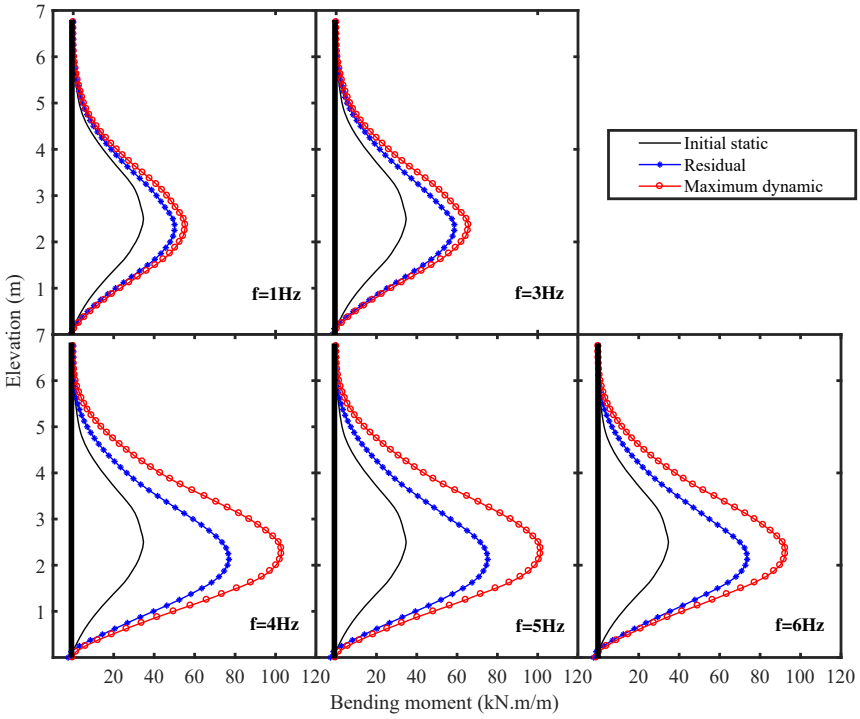

Fig. 22. Bending moment profiles along the sheetpile ($a_g = 0.1g$).

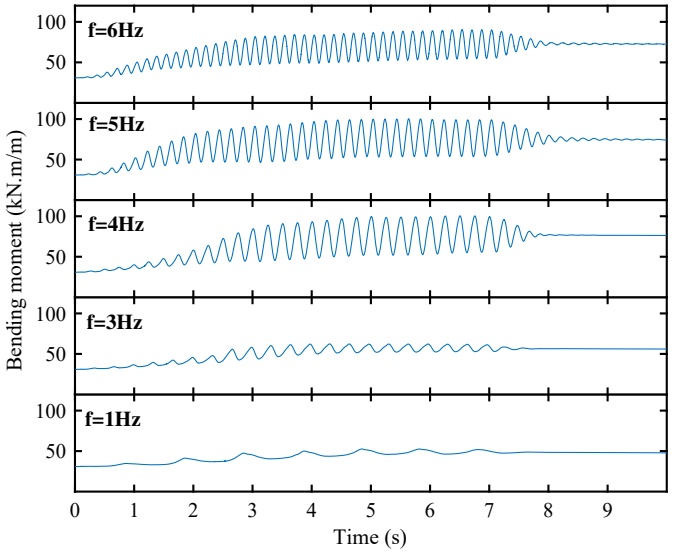

Fig. 23. Bending moment time histories at 2 m above sheetpile toe ($a_g = 0.1g$).

results of simulations with input motion frequencies of 4, 5, and 6 Hz show similar residual and maximum dynamic bending moments of approximately 75 and 100 kN · m/m, respectively. The results show that the input motion of 0.1g-1 Hz has the smallest maximum dynamic and residual bending moments, 55 and 50 kN · m/m, respectively. It is also evident from Fig. 22 that, in all cases, both the maximum dynamic and residual bending moments are significantly higher than the initial static moment. This was expected because of the higher dynamic and residual lateral earth pressure on the sheetpile.

The evolution of the bending moment during seismic loading at a maximum amplitude of 0.1 g and different frequencies at a point 2 m above the toe of the wall is shown in Fig. 23. The bending moment increases during the seismic loading, and the final residual moment is considerably higher than the initial static moment. This observation is consistent with the results of experiments conducted by other researchers (Finn et al. 1992; Madabhushi and Zeng 2006).

The initial static, maximum dynamic, and residual bending moments over the length of the sheetpile at a seismic excitation amplitude of 0.3 g and scaled earthquake motions are presented in Fig. 24. The results show that the residual bending moments are close to what was observed during the 0.1-g simulations at frequencies of 4–6 Hz. However, there is a noticeable increase in the dynamic bending moments over the results of the 0.1-g simulations, with the maximum moment corresponding to the 0.3g-4 Hz case, which is over 130 kN · m/m.

The maximum dynamic bending moment obtained from the DEM simulations at the input acceleration amplitude of 0.1 g with frequencies of 1, 3, and 4 Hz and input motion of 0.3g-4 Hz, along with those obtained using the analytical approach, are shown in Fig. 25. It is observed that for input motions of 0.1g-1 Hz and 0.1g-3 Hz there is close agreement between the results of the numerical and analytical solutions. In the case of 0.1g-1 Hz input motion, the maximum dynamic bending moments are 56 and 55.4 kN · m/m obtained from the analytical and numerical solutions, respectively, and the peak moment is located at almost the same elevation. According to the analytical method, for input motions of 0.1g-4 Hz and 0.3g-4 Hz (maximum surface accelerations of 0.46g and 0.65g behind the wall, respectively), the full strength of the soil in front of the wall is mobilized and the maximum bending moment over the length of the sheetpile is reached. However, the results of the DEM simulations show a much higher maximum bending moment for the 0.3g-4 Hz compared to 0.1g-4 Hz excitation. In this case the maximum bending moment is 132.2 kN · m/m, which is close to the maximum dynamic

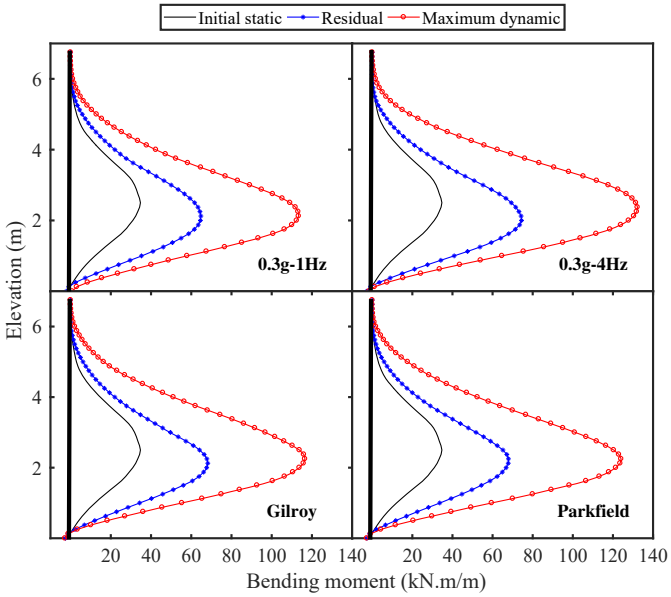

Fig. 24. Bending moment versus elevation for $a_g = 0.3g$ and scaled earthquakes.

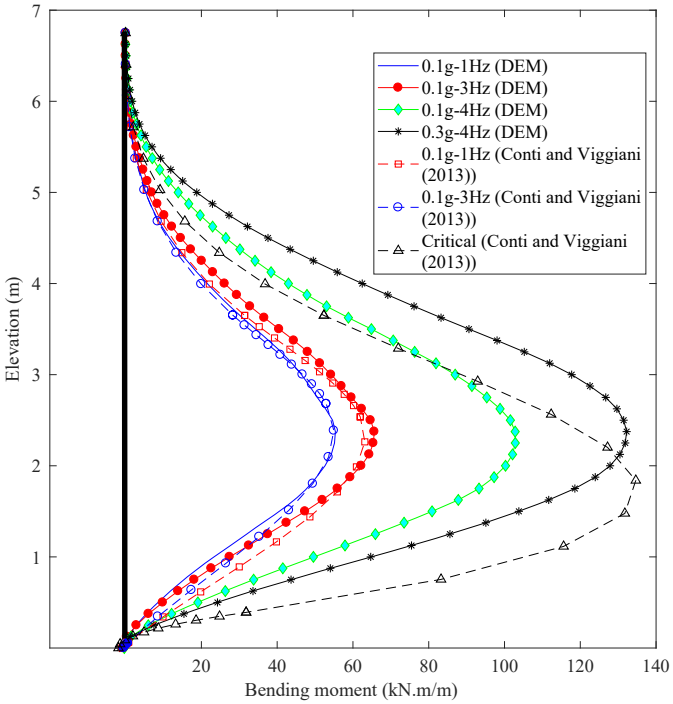

Fig. 25. Maximum dynamic bending moment obtained by DEM simulation and analytical solution.

moment, 134.7 kN · m/m, obtained using the Conti and Viggiani (2013) solution. Fig. 25 shows that the analytical solution predicts that the maximum bending moment is located at a lower point on the sheetpile compared to the DEM results. Conti and Viggiani (2013) observed a similar trend when the results of the analytical solution were compared against the data obtained from dynamic centrifuge tests conducted by Madabhushi and Zeng (2006). Their study showed that the maximum bending moments computed by the analytical method were close to the experimental data.

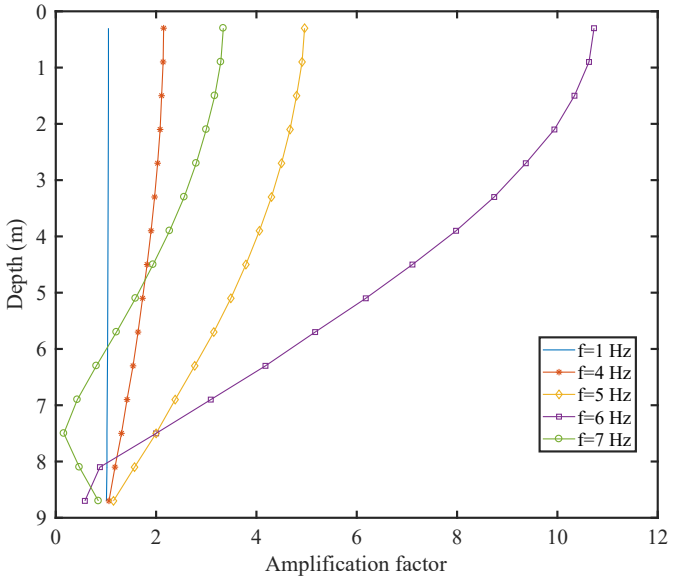

Fig. 26. Amplification factor inside free-field column versus depth ($a_g = 0.01g$).

Table 4. Amplification factors obtained from DEM solution and analytical expression (Eq. 6)

Input frequency (Hz)	Amplification factor (DEM)	Amplification factor (analytical)
1	1.05	1.04
4	2.15	2.11
5	4.96	4.4
6	10.73	10.4
7	3.34	3

However, for stronger ground accelerations, the analytical method predicts the point of maximum bending moment to be located deeper below dredge level compared to the experimental results.

Backfill Response

Amplification Factor

The horizontal accelerations in the direction of shaking at different depths of the deposit were monitored for all performed simulations. These accelerations were obtained by differentiating the average particle velocities within spherical volumes with radii of 6 mm (0.3 m in prototype units) positioned at several locations in the free-field column. Fig. 26 shows the profile of the amplification factors for the conducted simulations at an excitation amplitude of 0.01 g and different frequencies. The amplification factor is the ratio of the maximum soil horizontal acceleration at a specific depth location to the maximum input acceleration of the rigid base wall. The base input motion continued to propagate in the soil deposit and amplify toward the surface. The maximum amplification factor corresponds to the input acceleration frequency of 6 Hz, which is close to the fundamental frequency of the backfill (5.8 Hz). Table 4 shows a comparison of the amplification factors at the surface of the soil deposit computed from the DEM simulations (maximum acceleration of $0.01g$) and those of the analytical expression for the transfer of a shear wave propagating in linear elastic soil underlain by rigid bedrock (Kramer 1996). Using the transfer function, the amplification factor at the surface of the soil deposit is given by (Kramer 1996)

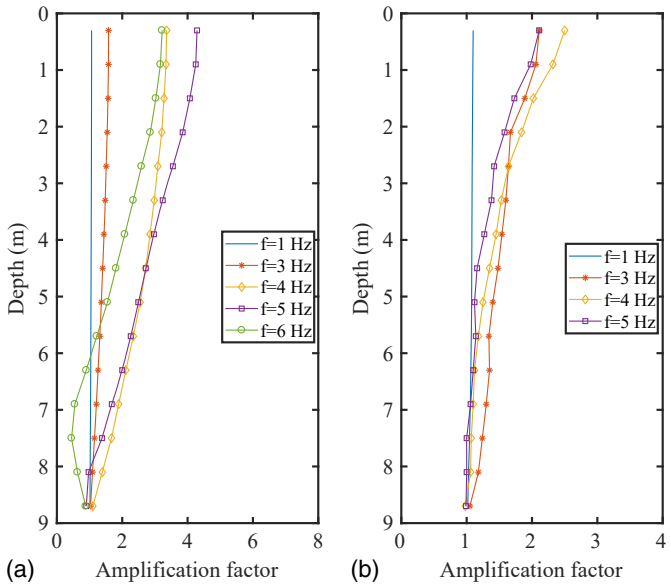

Fig. 27. Amplification factor inside free-field column versus depth: (a) $a_g = 0.1g$; and (b) $a_g = 0.3g$.

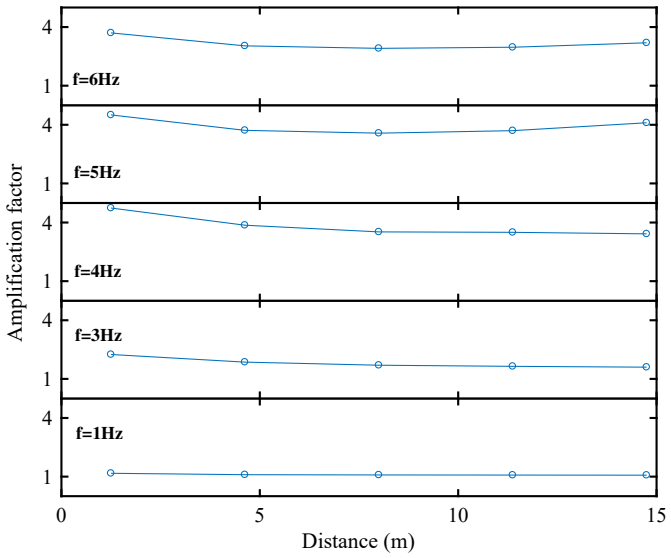

Fig. 28. Amplification factor near ground surface versus distance from sheetpile ($a_g = 0.1g$).

$$|F_2(\omega)| = \frac{1}{\sqrt{[\cos(\frac{\omega H}{V_s})]^2 + [\frac{\xi \omega H}{V_s}]^2}} \tag{6}$$

where ω = circular frequency of base excitation; H = total height of soil deposit; V_s = shear wave velocity; and ξ = damping ratio of soil deposit. Note that, in this equation, the parameters used in calculating the amplification factors are $H = 9$ m, $\xi = 5\%$, and $V_s = 210$ m/s. As can be seen from Table 4, there is close agreement between the results of the DEM simulations and the analytical solution. At maximum input motion amplitudes of 0.1 and 0.3 g, a decrease in the shear modulus and fundamental frequency of the deposit was expected, along with increased damping. The profiles of the amplification factors for the conducted simulations at excitation amplitudes of 0.1 and 0.3 g are presented in Fig. 27. It can be seen that the strongest amplifications of the input waves happen at frequencies of 5 and 4 Hz at excitation amplitudes of 0.1 and 0.3 g, respectively.

Fig. 28 shows the amplification factor near the ground surface as a function of distance from the sheetpile for the simulations with maximum input acceleration of $0.1g$. For the frequencies of 3–6 Hz, there is a noticeable increase in the amplification factor close to the sheetpile. It can be observed that, moving away from the sheetpile, the amplification factors converge to the values obtained near the top of the free-field column.

Backfill Failure Surface

Fig. 29 shows the development of maximum shear strain inside the soil deposit. To obtain the maximum shear strain at every location, strain rate tensors were tracked during the simulation within spherical volumes with a radius of 6 mm scattered every 12 mm (in model units) throughout the soil deposit. The strain tensors were computed by integrating the strain rate tensors at different locations. Eigenvalues of the shear strain tensors were calculated, and time histories for maximum shear strain at every location were determined.

Investigation of changes in maximum shear strain throughout the deposit revealed that a failure surface was formed during the simulation. In Fig. 29, the strain magnitude is demonstrated by different colors for the $0.1g$-5 Hz simulation. Fig. 29(a) shows the first sign of strain within the deposit occurring near the dredge line level behind the retaining wall. As the simulation progressed, the plane of maximum strain extended to the surface of the backfill, forming a failure slope [Fig. 29(b)]. The development of shear plane and failure wedge in the backfill can be observed in Figs. 29(c and d). It can also be seen that shear strain gradually develops on the excavation side. The wedges clearly resemble a Coulomb-like planar failure surface. Fig. 30 shows the particle displacement contour at the end of the $0.1g$-5 Hz simulation. Colors represent the magnitude of the total displacements. The failure soil wedges in front and back of the wall are evident in this figure. Clough and Duncan (1991) proposed that the ratio of maximum wall movement to the wall height, needed to reach minimum active and maximum passive earth pressure conditions, are 0.4% and 4%, respectively. For the case demonstrated in Fig. 30, this ratio is approximately 1.6%. This means that, according to Clough and Duncan (1991), the full active pressure of the backfill was mobilized while the wall did not undergo enough rotation to activate the full passive strength of the soil. The inclination of the formed active failure surface was determined to be around 44.5°. The measured angle was slightly lower than the analytical value of 47° obtained using Coulomb theory (Zarrabi-Kashani 1979).

Cyclic shear stress-strain loops at different locations inside the backfill for the $0.1g$-5 Hz simulation are presented in Fig. 31. The nonlinear behavior of the soil deposit is most noticeable at Points 1, 2, 5, and 6, which, according to Fig. 29, are located close to the areas of maximum strain. This was expected because these points are near the sheetpile where the failure surfaces developed. Owing to the large permanent strain observed inside the failure wedge, the soil exhibits nonlinear behavior that is reflected by the decrease in the angle of inclination of the stress-strain loops during the simulation, leading to lower stiffness and higher damping (area inside the loop). However, at the locations away from the sheetpile (Points 9 and 10), where strain levels are low, the inclination of the stress-strain loops is higher compared to the region close to the sheetpile, and consequently, the soil shows higher stiffness and lower damping. The effects of confining pressure can be clearly seen at Points

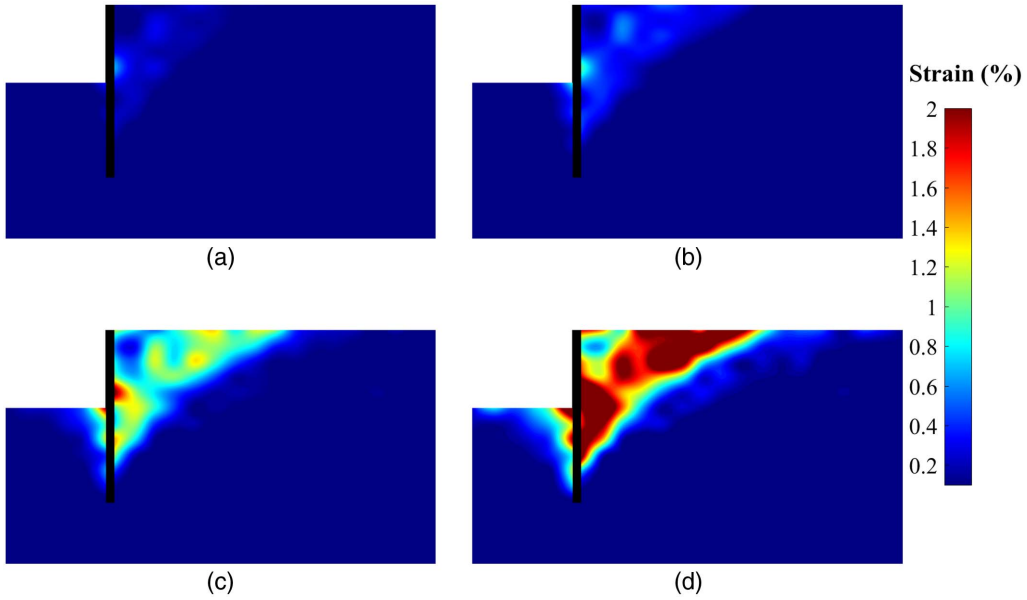

Fig. 29. Shear strain at different time instants during 0.1*g*-5 Hz simulation: (a) 1.5 s; (b) 2.0 s; (c) 3.5 s; and (d) 9.0 s.

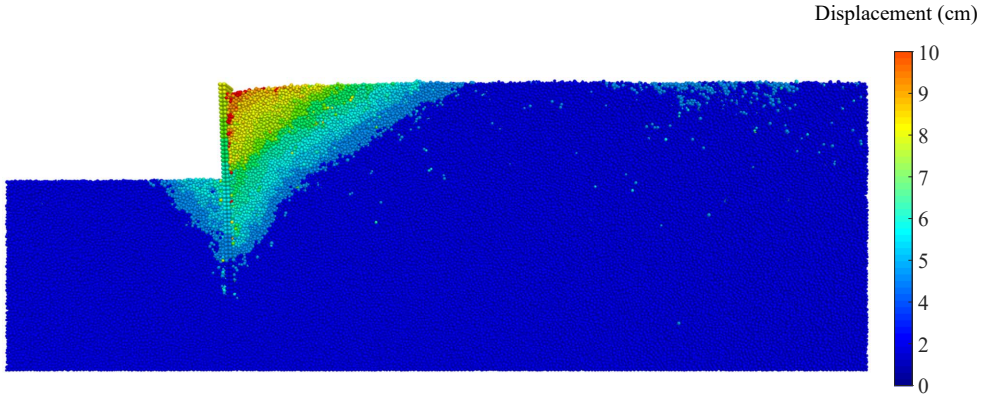

Fig. 30. Displacement contour at end of 0.1*g*-5 Hz simulation.

3, 4, 7, 8, 11, and 12 located near the base wall. A higher confining pressure at deeper levels leads to higher soil stiffness and smaller damping. This behavior is similar to that observed by Ishibashi and Zhang (1993) and Dobry and Vucetic (1987).

Ground Settlement

In addition to damage inflicted on the retaining walls during earthquakes, neighboring structures can also be affected by wall movements. A sheetpile can tilt or slide during the seismic excitation of a retaining wall/backfill system. Therefore, some ground settlement near the sheetpile is expected owing to wall rotation. To obtain the final ground settlement, the average vertical velocity of particles inside spherical volumes placed near the ground surface at different distances from the sheetpile were monitored during the simulation. The total ground settlements at different locations were calculated by integrating the average vertical velocities over the simulation time. Fig. 32 shows the results for the excitation amplitude of 0.1 g. Most of the ground settlement occurred near the sheetpile, and there is almost no settlement at distances more than 8 m from the sheetpile. The largest ground settlement corresponds to an input motion with a frequency close to the fundamental frequency of the backfill (5 Hz).

Fig. 33 shows the ground settlement at different distances from the sheetpile for the maximum input motion amplitude of 0.3 g and scaled earthquake records. It is evident that the ground settlements are significantly larger for input motion of 0.3*g*-4 Hz. In this case, the ground experiences a maximum settlement of more than 18 cm near the retaining wall.

Conclusions

A DEM microscale approach is presented to evaluate the seismic response of a cantilever retaining wall/backfill system in the time domain. The presented approach accounts for several factors, such as the nonlinear behavior of soil, dynamic soil–retaining wall interaction, sliding and rotation of the sheetpile, possible separation between sheetpile and backfill motions, and dynamic characteristics of the flexible retaining wall. Pressure distributions on the sides of the wall change with the wall rotation, and as the wall tilts the full

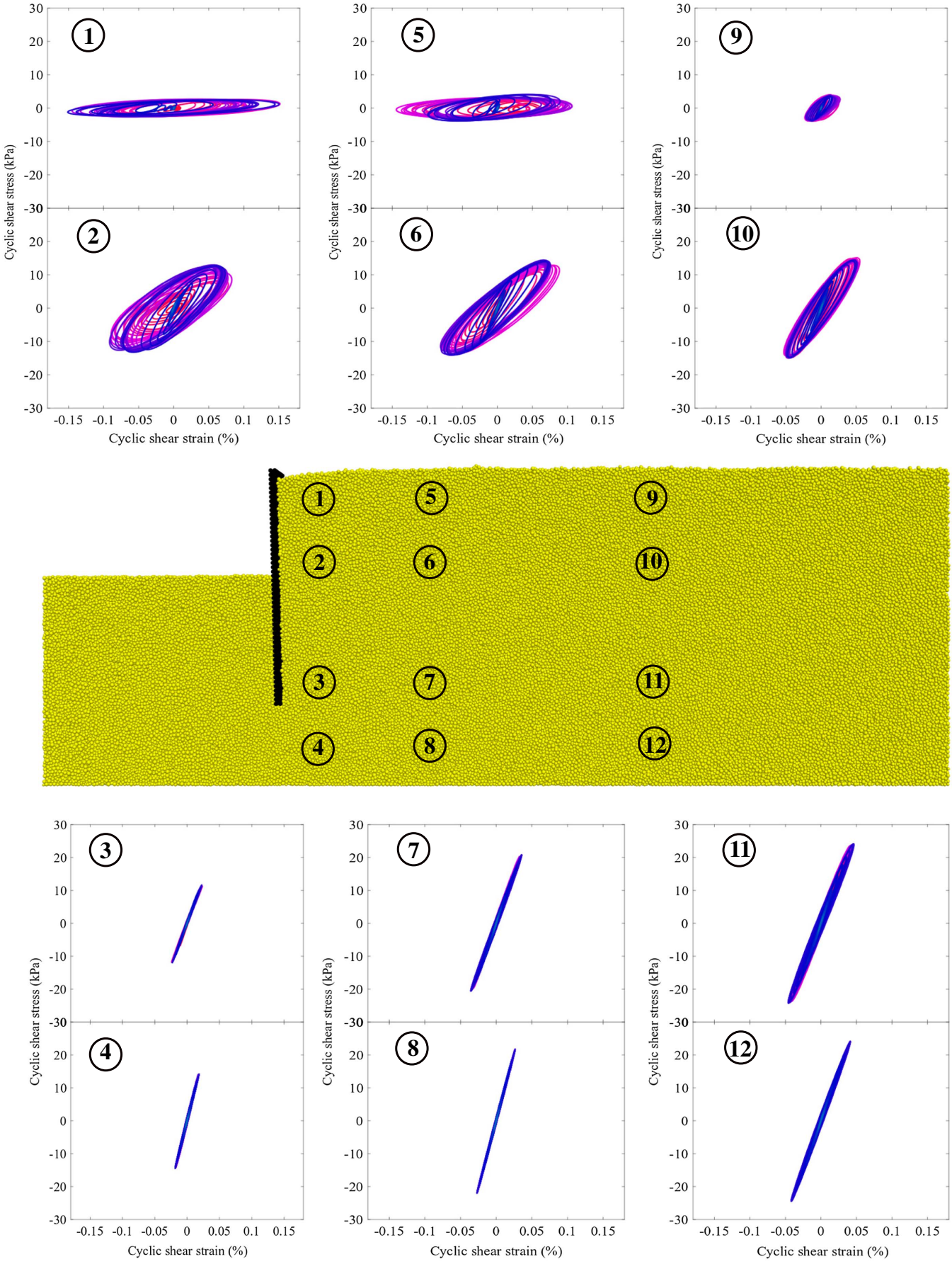

Fig. 31. Cyclic shear stress-strain loops at different locations behind wall in the 0.1*g*-5 Hz simulation.

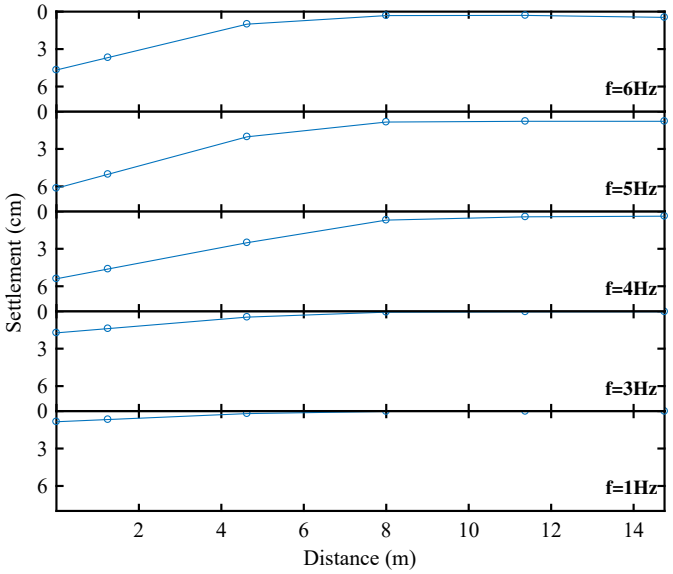

Fig. 32. Ground settlement versus distance from sheetpile ($a_g = 0.1g$).

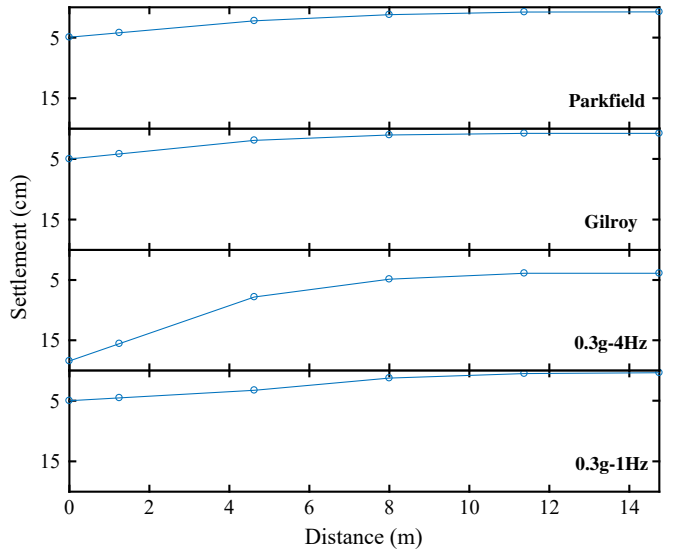

Fig. 33. Ground settlement versus distance from sheetpile for $a_g = 0.3g$ and scaled earthquakes.

strength of the soil in a larger region of the soil on the excavated side becomes mobilized. The mobilization of the passive strength of the soil in front of the sheetpile continues down to about half the embedded length of the wall, and the critical state was never observed during the conducted simulations. The results show that the maximum dynamic and residual passive lateral earth pressures and bending moments on the sheetpile are considerably higher than the initial static values and could be as high as four to six times the static values. For ground acceleration stronger than the critical limit, the maximum lateral earth pressure stays almost at a constant level. However, the maximum dynamic bending moment on the wall is found to increase even for ground accelerations higher than the critical value. Failure wedges are formed in front of and behind the sheetpile during the seismic loading and become larger as the simulation progresses. This is accompanied by ground settlement in the backfill, especially near the sheetpile. In addition, it was found that the maximum amplification of ground acceleration behind the sheetpile, the amount of deformation the wall experienced, and the maximum level of its internal forces and moments during dynamic loading were strongly affected by the frequency and amplitude of the input motion.

The main goal of this study was to examine the potential of a DEM to analyze the response of soil–retaining wall systems subjected to dynamic loading. The obtained results highlight the strength of the proposed DEM-based approach and its ability to model large-scale boundary value problems. The trends observed in this study were similar to published experimental and analytical results. One of the biggest advantages of this method is its seamless nature in the sense that the input parameters can be physically interpreted and do not change with the change in the simulated deposit and wall. While the presented computational framework is successful at capturing key aspects of the complicated dynamic behavior of soil–retaining wall systems, further studies with regard to the influence of various parameters, such as particle size, stiffness, and packing porosity, on the response of the system are needed and left for future work.

Data Availability Statement

Some or all data, models, or code that support the findings of this study are available from the corresponding author upon reasonable request (simulation output and MATLAB codes used for processing the data).

Acknowledgments

The authors would like to thank the anonymous reviewers for their valuable remarks that helped improve this manuscript. This research was partially supported by the US Army Corps of Engineers Engineer Research and Development Center, Grant No. W9132V-13-C-0004, and the National Science Foundation Award No. CMMI-1728612. This support is gratefully acknowledged.

References

Al Atik, L., and N. Sitar. 2010. "Seismic earth pressures on cantilever retaining structures." *J. Geotech. Geoenviron. Eng.* 136 (10): 1324–1333. https://doi.org/10.1061/(ASCE)GT.1943-5606.0000351.

Al-Homoud, A. S., and R. V. Whitman. 1990. "Evaluating tilt of gravity retaining walls during earthquakes." Ph.D. thesis, Dept. of Civil Engineering, Massachusetts Institute of Technology.

Bakr, J., and S. M. Ahmad. 2018. "A finite element performance-based approach to correlate movement of a rigid retaining wall with seismic earth pressure." *Soil Dyn. Earthquake Eng.* 114 (Nov): 460–479. https://doi.org/10.1016/j.soildyn.2018.07.025.

Bardet, J.-P. 1994. "Observations on the effects of particle rotations on the failure of idealized granular materials." *Mech. Mater.* 18 (2): 159–182. https://doi.org/10.1016/0167-6636(94)00006-9.

Bardet, J.-P., and Q. Huang. 1992. "Numerical modeling of micropolar effects in idealized granular materials." *Mech. Granular Mater. Powder Syst.* 37: 85–91.

Cakir, T. 2013. "Evaluation of the effect of earthquake frequency content on seismic behavior of cantilever retaining wall including soil–structure interaction." *Soil Dyn. Earthquake Eng.* 45 (Feb): 96–111. https://doi.org/10.1016/j.soildyn.2012.11.008.

Callisto, L., and F. M. Soccodato. 2007. "Seismic analysis of an embedded retaining structure in coarse-grained soils." In *Proc. 4th Int. Conf. on Earthquake Gotechnical Engineering*, 25–28. Dordrecht, Netherlands: Springer.

Caltabiano, S., E. Cascone, and M. Maugeri. 2012. "Static and seismic limit equilibrium analysis of sliding retaining walls under different surcharge conditions." *Soil Dyn. Earthquake Eng.* 37 (Jun): 38–55. https://doi.org/10.1016/j.soildyn.2012.01.015.

Calvetti, F., G. Combe, and J. Lanier. 1997. "Experimental micromechanical analysis of a 2D granular material: Relation between structure evolution and loading path." *Mech. Cohesive-Frictional Mater.* 2 (2): 121–163. https://doi.org/10.1002/(SICI)1099-1484(199704)2:2<121::AID-CFM27>3.0.CO;2-2.

Chang, C. S., and S.-J. Chao. 1994. "Discrete-element analysis for active and passive pressure distribution on retaining wall." *Comput. Geotech.* 16 (4): 291–310. https://doi.org/10.1016/0266-352X(94)90012-4.

Chopra, A. K. 2017. *Dynamics of structures: Theory and applications to earthquake engineering*. Hoboken, NJ: Pearson.

Clough, G., and J. Duncan. 1991. "Earth pressures." In *Foundation engineering handbook*, 223–235. New York: Springer.

Collin, J. 1992. "Field observation of reinforced soil structures under seismic loading." In *Proc., Earth Reinforcement Practice*, 223–228. Rotterdam, Netherlands: A.A. Balkema.

Conti, R., G. Madabhushi, and G. Viggiani. 2012. "On the behaviour of flexible retaining walls under seismic actions." *Géotechnique* 62 (12): 1081. https://doi.org/10.1680/geot.11.P.029.

Conti, R., and G. M. Viggiani. 2013. "A new limit equilibrium method for the pseudostatic design of embedded cantilevered retaining walls." *Soil Dyn. Earthquake Eng.* 50 (Jul): 143–150. https://doi.org/10.1016/j.soildyn.2013.03.008.

Cundall, P. A., and O. D. Strack. 1979. "A discrete numerical model for granular assemblies." *Géotechnique* 29 (1): 47–65. https://doi.org/10.1680/geot.1979.29.1.47.

Dobry, R., and T. Ng. 1992. "Discrete modelling of stress-strain behaviour of granular media at small and large strains." *Eng. Comput.* 9 (2): 129–143. https://doi.org/10.1108/eb023853.

Dobry, R., and M. Vucetic. 1987. *Dynamic properties and seismic response of soft clay deposits.* Troy, NY: Rensselaer Polytechnic Institute.

El Shamy, U., and F. Aydin. 2008. "Multiscale modeling of flood-induced piping in river levees." *J. Geotech. Geoenviron. Eng.* 134 (9): 1385–1398. https://doi.org/10.1061/(ASCE)1090-0241(2008)134:9(1385).

El Shamy, U., and M. Zeghal. 2005. "Coupled continuum-discrete model for saturated granular soils." *J. Eng. Mech.* 131 (4): 413–426. https://doi.org/10.1061/(ASCE)0733-9399(2005)131:4(413).

Evans, T. M., and J. D. Frost. 2010. "Multiscale investigation of shear bands in sand: Physical and numerical experiments." *Int. J. Numer. Anal. Methods Geomech.* 34 (15): 1634–1650. https://doi.org/10.1002/nag.877.

Fang, Y., Y. Yang, and T. Chen. 2003. "Retaining walls damaged in the Chi-Chi earthquake." *Can. Geotech. J.* 40 (6): 1142–1153. https://doi.org/10.1139/t03-055.

Finn, W. L., G. Wu, and N. Yoshida. 1992. "Seismic response of sheet pile walls." In Vol. 3 of *Proc., Materiały: 10th World Conf. on Earthquake Engineering, Madryt*, 1689–1694. Rotterdam, Netherlands: A.A. Balkema.

Gazetas, G., E. Garini, and A. Zafeirakos. 2016. "Seismic analysis of tall anchored sheet-pile walls." *Soil Dyn. Earthquake Eng.* 91: 209–221. https://doi.org/10.1016/j.soildyn.2016.09.031.

Grivas, D., and C. Souflis. 1984. "Performance of the Plateas wingwall during the 1981 earthquakes in Greece." In Vol. 3 of *Proc., 8th World Conf. on Earthquake Engineering*, 509–515. Upper Saddle River, NJ: Prentice Hall.

Huang, C.-C., and Y.-H. Chen. 2004. "Seismic stability of soil retaining walls situated on slope." *J. Geotech. Geoenviron. Eng.* 130 (1): 45–57. https://doi.org/10.1061/(ASCE)1090-0241(2004)130:1(45).

Iai, S., T. Tobita, and T. Nakahara. 2005. "Generalised scaling relations for dynamic centrifuge tests." *Géotechnique* 55 (5): 355–362. https://doi.org/10.1680/geot.2005.55.5.355.

Ishibashi, I., and X. Zhang. 1993. "Unified dynamic shear moduli and damping ratios of sand and clay." *Soils Found.* 33 (1): 182–191. https://doi.org/10.3208/sandf1972.33.182.

Itasca, C. 2019. *PFC3D (particle flow code in 3 dimensions), version 6.0*. Minneapolis: Itasca Consulting Group.

Iwashita, K., and M. Oda. 1998. "Rolling resistance at contacts in simulation of shear band development by Dem." *J. Eng. Mech.* 124 (3): 285–292. https://doi.org/10.1061/(ASCE)0733-9399(1998)124:3(285).

Jiang, M., J. He, J. Wang, F. Liu, and W. Zhang. 2014. "Distinct simulation of earth pressure against a rigid retaining wall considering inter-particle rolling resistance in sandy backfill." *Granular Matter* 16 (5): 797–814. https://doi.org/10.1007/s10035-014-0515-3.

Ko, Y.-Y., and H.-H. Yang. 2019. "Deriving seismic fragility curves for sheet-pile wharves using finite element analysis." *Soil Dyn. Earthquake Eng.* 123 (Oct): 265–277. https://doi.org/10.1016/j.soildyn.2019.05.014.

Kramer, S. 1996. *Geotechnical earthquake engineering*. Upper Saddle River, NJ: Prentice Hall.

Kramer, S. L., and M. W. Smith. 1997. "Modified Newmark model for seismic displacements of compliant slopes." *J. Geotech. Geoenviron. Eng.* 123 (7): 635–644. https://doi.org/10.1061/(ASCE)1090-0241(1997)123:7(635).

Lancellotta, R. 2002. "Analytical solution of passive earth pressure." *Géotechnique* 52 (8): 617–619. https://doi.org/10.1680/geot.2002.52.8.617.

Lancellotta, R. 2007. "Lower-bound approach for seismic passive earth resistance." *Géotechnique* 57 (3): 319–321. https://doi.org/10.1680/geot.2007.57.3.319.

Lin, Y.-L., X.-M. Cheng, G.-L. Yang, and Y. Li. 2018. "Seismic response of a sheet-pile wall with anchoring frame beam by numerical simulation and shaking table test." *Soil Dyn. Earthquake Eng.* 115 (Dec): 352–364. https://doi.org/10.1016/j.soildyn.2018.07.028.

Lysmer, J., and R. L. Kuhlemeyer. 1969. "Finite dynamic model for infinite media." *J. Eng. Mech. Div.* 95 (4): 859–878.

Madabhushi, S., and X. Zeng. 2006. "Seismic response of flexible cantilever retaining walls with dry backfill." *Geomech. Geoeng. Int. J.* 1 (4): 275–289. https://doi.org/10.1080/17486020601039170.

Madabhushi, S., and X. Zeng. 2007. "Simulating seismic response of cantilever retaining walls." *J. Geotech. Geoenviron. Eng.* 133 (5): 539–549. https://doi.org/10.1061/(ASCE)1090-0241(2007)133:5(539).

Misra, A., and H. Jiang. 1997. "Measured kinematic fields in the biaxial shear of granular materials." *Comput. Geotech.* 20 (3–4): 267–285. https://doi.org/10.1016/S0266-352X(97)00006-2.

Mononobe, N. 1929. "On determination of earth pressure during earthquake." In Vol. 9 of *Proc., World Engineering Congress*, 177–185. Tokyo: World Engineering Congress.

Nadim, F., and R. V. Whitman. 1983. "Seismically induced movement of retaining walls." *J. Geotech. Eng.* 109 (7): 915–931. https://doi.org/10.1061/(ASCE)0733-9410(1983)109:7(915).

Nadukuru, S. S., and R. L. Michalowski. 2012. "Arching in distribution of active load on retaining walls." *J. Geotech. Geoenviron. Eng.* 138 (5): 575–584. https://doi.org/10.1061/(ASCE)GT.1943-5606.0000617.

Newmark, N. M. 1965. "Effects of earthquakes on dams and embankments." *Géotechnique* 15 (2): 139–160. https://doi.org/10.1680/geot.1965.15.2.139.

Oda, M., J. Konishi, and S. Nemat-Nasser. 1982. "Experimental micromechanical evaluation of strength of granular materials: Effects of particle rolling." *Mech. Mater.* 1 (4): 269–283. https://doi.org/10.1016/0167-6636(82)90027-8.

Oetomo, J. J., E. Vincens, F. Dedecker, and J.-C. Morel. 2016. "Modeling the 2D behavior of dry-stone retaining walls by a fully discrete element method." *Int. J. Numer. Anal. Methods Geomech.* 40 (7): 1099–1120. https://doi.org/10.1002/nag.2480.

Okabe, S. 1926. "General theory of earth pressures." *J. Japan Soc. Civ. Eng.* 12 (1).

Osouli, A., and S. Zamiran. 2017. "The effect of backfill cohesion on seismic response of cantilever retaining walls using fully dynamic analysis." *Comput. Geotech.* 89 (Sep): 143–152. https://doi.org/10.1016/j.compgeo.2017.04.007.

O'Sullivan, C. 2011. *Particulate discrete element modelling: A geomechanics perspective*. London: CRC Press.

Pitilakis, K., and A. Moutsakis. 1989. "Seismic analysis and behaviour of gravity retaining walls—The case of Kalamata harbour quaywall." *Soils Found.* 29 (1): 1–17. https://doi.org/10.3208/sandf1972.29.1.

Psarropoulos, P., G. Klonaris, and G. Gazetas. 2005. "Seismic earth pressures on rigid and flexible retaining walls." *Soil Dyn. Earthquake Eng.* 25 (7–10): 795–809. https://doi.org/10.1016/j.soildyn.2004.11.020.

Radjaï, F., and F. Dubois. 2011. *Discrete-element modeling of granular materials*. New York: Wiley.

Richards, R., Jr., and D. G. Elms. 1979. "Seismic behavior of gravity retaining walls." *J. Geotech. Eng. Div.* 105 (4): 449–464.

Tateyama, M., F. Tatsuoka, J. Koseki, and K. Horii. 1995. "Damage to soil retaining walls for railway embankments during the great Hanshin-Awaji earthquake, January 17, 1995." In *Earthquake Geotechnical Engineering*. Rotterdam, Netherlands: A.A. Balkema.

Tatsuoka, F., M. Tateyama, and J. Koseki. 1996. "Performance of soil retaining walls for railway embankments." *Soils Found.* 36 (Special): 311–324. https://doi.org/10.3208/sandf.36.Special_311.

Thornton, C. 2000. "Numerical simulations of deviatoric shear deformation of granular media." *Géotechnique* 50 (1): 43–53. https://doi.org/10.1680/geot.2000.50.1.43.

Trandafir, A. C., T. Kamai, and R. C. Sidle. 2009a. "Earthquake-induced displacements of gravity retaining walls and anchor-reinforced slopes." *Soil Dyn. Earthquake Eng.* 29 (3): 428–437. https://doi.org/10.1016/j.soildyn.2008.04.005.

Wartman, J., J. D. Bray, and R. B. Seed. 2003. "Inclined plane studies of the Newmark sliding block procedure." *J. Geotech. Geoenviron. Eng.* 129 (8): 673–684. https://doi.org/10.1061/(ASCE)1090-0241(2003)129:8(673).

White, W., I. K. Lee, and S. Valliappan. 1977. "Unified boundary for finite dynamic models." *J. Eng. Mech. Div.* 103 (5): 949–964.

Whitman, R. V., and S. Liao. 1985. *Seismic design of gravity retaining walls*. Vicksburg, MI: Dept. of Civil Engineering, Massachusetts Institute of Technology.

Zamani, N., and U. El Shamy. 2011. "Analysis of wave propagation in dry granular soils using DEM simulations." *Acta Geotech.* 6 (3): 167. https://doi.org/10.1007/s11440-011-0142-7.

Zamani, N., and U. El Shamy. 2012. "Analysis of the seismic response of soil–foundation–structure systems using a microscale framework." *Soil Dyn. Earthquake Eng.* 43 (Dec): 398–412. https://doi.org/10.1016/j.soildyn.2012.07.010.

Zarrabi-Kashani, K. 1979. "Sliding of gravity retaining wall during earthquakes considering vertical acceleration and changing inclination of failure surface." Ph.D. thesis, Dept. of Civil Engineering, Massachusetts Institute of Technology.

Zeng, X. 1990. "Modelling the behaviour of quay walls in earthquakes." Ph.D. thesis, Dept. of Engineering, Civil Engineering Div., Univ. of Cambridge.

Zeng, X., and R. Steedman. 1993. "On the behaviour of quay walls in earthquakes." *Géotechnique* 43 (3): 417–431. https://doi.org/10.1680/geot.1993.43.3.417.

Zeng, X., and R. Steedman. 2000. "Rotating block method for seismic displacement of gravity walls." *J. Geotech. Geoenviron. Eng.* 126 (8): 709–717. https://doi.org/10.1061/(ASCE)1090-0241(2000)126:8(709).

Zienkiewicz, O., N. Bicanic, and F. Shen. 1989. "Earthquake input definition and the trasmitting boundary conditions." In *Advances in computational nonlinear mechanics*, 109–138. New York: Springer.